LAL/RT 90-14
December 1990

Laboratoire de l'Accélérateur Linéaire

A Beam Size Monitor for the Final Focus Test Beam

J. Buon, F. Couchot, J. Jeanjean, F. Le Diberder, V. Lepeltier, H. Nguyen Ngoc, J. Perez-y-Jorba and P. Puzo

Laboratoire de l'Accélérateur Linéaire
IN2P3-CNRS et Université de Paris-Sud
F-91405 Orsay Cedex, France

and

P. Chen
Stanford Linear Accelerator Center, Stanford

Submitted to Nuclear Instruments and Methods

U.E.R
de
l'Université Paris-Sud

Institut National
de Physique Nucléaire
et
de Physique des Particules

Bâtiment 200 - 91405 ORSAY Cedex

LAL/RT 90-14
December 1990

A Beam Size Monitor for the Final Focus Test Beam

J. Buon, F. Couchot, J. Jeanjean, F. Le Diberder, V. Lepeltier, H. Nguyen Ngoc, J. Perez-y-Jorba and P. Puzo

Laboratoire de l'Accélérateur Linéaire
IN2P3-CNRS et Université de Paris-Sud
F-91405 Orsay Cedex, France

and

P. Chen
Stanford Linear Accelerator Center, Stanford

Abstract:

The beam size monitor, proposed here to be installed at the focus of FFTB, will be made of a pulsed gas target and an ion detector. The gas is ionized by the beam and the ions are kicked by its space charge field. The time of flight of Ar^+ ions up to the detector and the angular distribution of He^+ ions will allow to obtain the two beam transverse dimensions in the range of the FFTB design.

1. Introduction

A beam size monitor is an essential instrument for the Final Focus Test Beam[1] (FFTB) in construction at SLAC*. Conventional methods would not work to measure the transverse bunch dimensions at the focus where they range from 1 μm down to 60 nm.

The method, proposed here, follows the initial ideas of J. Rees[2] and C. Prescott[3] for the SLC beams, that were extended by J. Buon[4] and P. Chen[5] to the case of flat beams for the FFTB. Ions are created by the electron bunch in a gas at the focus. *Essentially, the information on the transverse dimensions is obtained through the kick given to the ions by the space charge electric field of the bunch.* After passage of the bunch, the ions are emitted in the transverse plane and are collected by an ion detector.

In the case of *heavy* ions, that move only slightly during the bunch passage, their maximum velocity is proportional to the maximum electric field. The latter is inversely proportional to the largest transverse beam dimension, namely the horizontal dimension. *The measurement of the time of flight of the ions from the focus to the detector will give this horizontal dimension.*

In the case of *light* ions, that are trapped by the electron bunch and oscillate in its potential well, their oscillation amplitude depends on their initial position. In a horizontally flat bunch, the horizontal amplitude and the final horizontal ion velocity are in average larger than the vertical ones. The angular distribution is peaked along the horizontal direction of the transverse plane. On the contrary the angular distribution is isotropic for a round beam. *The measurement of the angular distribution will give the bunch aspect ratio.* It will also be used to correct the measurement of the horizontal dimension with heavy ions that has a relatively weak dependence on the aspect ratio. This measurement requires that the FFTB should be operated with electrons only.

It is worth noting that these measurements are not biased by any beam jitter. It also means that they cannot give any useful information on the beam position.

For clear experimental reasons the best choice is *Argon* as heavy ions and *Helium* as light ions.

The ionization of a gas by the FFTB beam is studied in Section 2. The ionization process is caracterized by large impact parameters and by a limited coherence length of the photons exchanged with the atoms. It is a situation very different from the usual ionization process in an extended and dense medium at lower beam energies.

The *space charge electric and magnetic fields* of an electron bunch at the focus are studied in Section 3. The kick received by the ions is mainly due to the transverse electric component.

---

* The FFTB is a DESY (Hamburg), INP (Novosibirsk), KEK (Tsukuba), LAL (Orsay) and SLAC (Stanford) collaboration.

A computer *code* has been developped to simulate the ionization by the electron beam and the motion of the ions in the space charge field (see Appendix I).

The *detailed study and the numerical results* of the code are given in Section 4 for heavy Argon ions and in Section 5 for light Helium ions in the case of an electron beam. The case of a positron beam is studied in Section 6.

The principle of the *experimental set-up* is described in Section 7.

Possible *backgrounds* are investigated in Section 8.

The *experimental resolution* and the operation conditions, that result from a simulation of the apparatus, are discussed in Section 9.

Finally, the possible extension of the method to the case of a *future electron-positron linear collider* NLC is studied in Section 10.

In conclusion, from the present study it is expected that the method will work in the range of the FFTB dimensions, from the largest beam aspect ratio, about R=16, to the limit of wire scanners (≈ 2 μm with a few 10^9 electrons).

2. Gas ionization by the FFTB beam.

No experimental data exist on ionization by a 50 GeV electron beam passing through a thin gas target. One must calculate the ionization cross-section by relating it to data on photo-ionization cross-section[6]. A detailed study is given in Appendix II.

The ionization cross-section is the sum of two contributions : the Rutherford cross-section of point-like interaction and the cross-section of resonant interaction with the atom.

At ultrarelativistic energies the resonant cross-section differential with respect to the energy ω of the virtual photon, exchanged between the electron and the atom, is given by :

$$\frac{d\sigma}{d\omega} = \frac{\alpha}{\pi}\frac{\sigma_\gamma(\omega)}{\omega} Ln\left(\frac{2m_e c^2 \gamma_e^2}{\omega}\right)$$

where $\sigma_\gamma(\omega)$ is the photo-ionization cross-section, γ_e is the electron Lorentz factor, m_e is its mass and α is the fine structure constant.

At high energy the differential Rutherford cross-section is much smaller than the resonant cross-section and is approximatively given by :

$$\frac{d\sigma}{d\omega} = 2\pi r_e^2 \frac{m_e c^2}{\omega^2}$$

per quasi-free atomic electron, i.e. with an ionization energy ω_I smaller than ω (r_e is the electron classical radius).

Table I gives the calculated ionization cross-sections (integrated over ω) for He and Ar at 50 GeV and at the minimum energy loss ($\beta\gamma = 4$) for comparison with the number of primary ionization events that are known[7] in these gases.

$\beta\gamma$			He	Ar
4	σ_i	:	0.13 Mb	1.1 Mb
4	n_p	:	3.5 cm^{-1}	29 cm^{-1}
10^5	σ_i	:	0.3 Mb	2.4 Mb
10^5	$b_{max}^{(0)}$	:	0.67 mm	1 mm

Table I : The calculated total ionization cross-section σ_i, the number n_p of primary events per cm at NTP and the maximum impact parameter $b_{max}^{(0)}$ for He and Ar, without any limitation on the coherence length of the exchanged photons.

At high energy the resonant ionization is partly due to distant collisions between the electron and the atom. The distribution of impact parameters b (i.e. the closest distance of approach) roughly scales as 1/b, from b_{min} ≈ atomic radius to $b_{max}^{(0)}$ given in Table I.

At high energy ($\gamma >> 1$), when the maximum impact parameter is much larger than the atomic radius, one can use a semiclassical picture : an incident electron emits a quasi-real photon. The photon propagates up to an atom that is ionized.

The maximum impact parameter is in fact limited by the maximum flight distance of the exchanged photon. As virtual photons are mainly emitted in the forward direction and cannot propagate far away in the transverse direction, the flight distance cannot be larger than the distance l^* to the last bending of the electron trajectory[8]. In the case of FFTB this distance is about the distance from the last quadrupole QC1 to the focus : $l^* \approx 50$ cm.

The differential resonant cross-section is reduced and given by :

$$\frac{d\sigma}{d\omega} = \frac{\alpha}{\pi} \frac{\sigma_\gamma(\omega)}{\omega} Ln\left(\frac{2l^*}{\lambda\!\!\!^{-}_c}\right)$$

where $\lambda\!\!\!^{-}_c$ is the Compton wavelength (divided by 2π).

Table II gives the effective maximum impact parameter $b_{max}^{(1)}$ and the total cross-section for He and Ar at 50 GeV.

		He	Ar
ω	:	30 eV	20 eV
$b_{max}^{(1)}$	:	60 μm	70 μm
σ_i	:	0.27 Mb	2.0 Mb

Table II : The maximum impact parameter $b_{max}^{(1)}$ for a typical exchanged-photon energy ω, and the total ionization cross-section limited by the flight distance l^* in the case of FFTB.

Finally, as the electron density in the bunch is very large, there is some probability of successive ionizations of the same atom. There is also some probability of a direct production of a multi-charged ion in a single ionization event.

All the needed ionization cross-sections are given in table III. They have been estimated as explained in Appendix II.

$\sigma_{ut}(He \rightarrow He^{+})$	= 0.267 Mb	$\sigma_{ut}(Ar \rightarrow Ar^{+})$	= 2.01 Mb
$\sigma_{ut}(He^{+} \rightarrow He^{2+})$	= 0.048 Mb	$\sigma_{ut}(Ar^{+} \rightarrow Ar^{2+})$	= 1.24 Mb
$\sigma_{ut}(He \rightarrow He^{2+})$	≈ 445 b	$\sigma_{ut}(Ar \rightarrow Ar^{2+})$	= 0.02 Mb
		$\sigma_{ut}(Ar^{2+} \rightarrow Ar^{3+})$	= 0.56 Mb

Table III : Total estimated ionization cross-sections for He and Ar.

It is assumed that the threshold for tunnelling ionization[9] by the space charge field is not yet reached for FFTB, although it could be reached by some increase of the electron density in the bunch. Tunnelling ionization would be dominant in the case of a NLC and would considerably change the situation (see Section 10).

Now, a saturation of gas ionization can be reached when the electron density in the bunch is very large. Usually, the number N_i of ions produced per cm in a gas target of density n_g is simply given by :

$$N_i = N_e \, n_g \, \sigma_i$$

as function of the number of electrons N_e and of the ionization cross-section σ_i. However, for pointlike interaction, this number N_i cannot be larger than the number of atoms in the gas section crossed by the beam. The latter decreases when the beam cross-section is decreased. A saturation is reached when both numbers are equal. In the saturation regime the number of ions becomes proportional to the beam cross-section[5]. In principle, the counting rate of ions could be used to obtain the beam dimensions in the saturation regime. However, the long tail of the impact parameter distribution implies that a fraction of the ions are created outside the beam core (see Figure 1) and that saturation is largely reduced. Figure 2 illustrates the reduction of saturation for Argon (in any case saturation could not be reached for Helium as the ionization cross-section is much smaller).

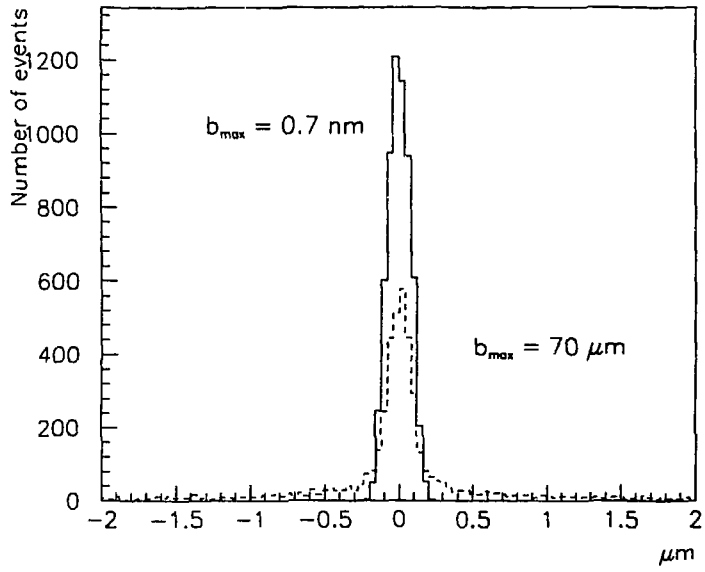

Figure 1 : The vertical distribution of Argon atoms, ionized by a flat beam, for two values of the maximum impact parameter b_{max} = 70 μm and 0.7 nm (the number of ions are normalized to the same value in both cases). Horizontal dimension : σ_x = 1 μm, vertical dimension : σ_y = 0.06 μm and $N_e = 10^{10}$ incident electrons.

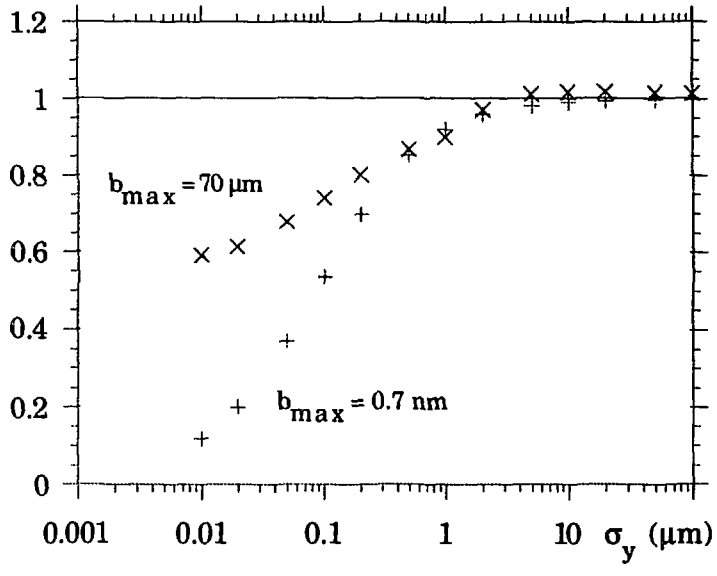

Figure 2 : The number of Argon ions, produced per cm in a target of density n_g and normalized to $N_i = N_e\, n_g\, \sigma_i$, versus the vertical beam dimension σ_y, as given by the simulation code (σ_x = 1 μm and $N_e = 10^{10}$). The two sets of points correspond to two values of the maximum impact parameter b_{max} = 70 μm and 0.7 nm.

Moreover, multiple ionization can be significant in the case of Argon. Figure 3 shows the variation of the estimated percentage of Ar^{2+} ions produced by multiple ionization. It would reach 15 % at an aspect ratio of 16. It would hardly allow an absolute measurement of the beam dimensions, due to the uncertainty on the ionization cross-sections. A relative measurement, based on the variation of the Ar^{+} and Ar^{2+} counting rates, may be possible if the background level is not too high.

The percentage of Ar^{3+} is only 3.5 % at most and can be neglected. Similarly, in the case of Helium, the percentage of He^{2+} is 2 % at most and is negligible.

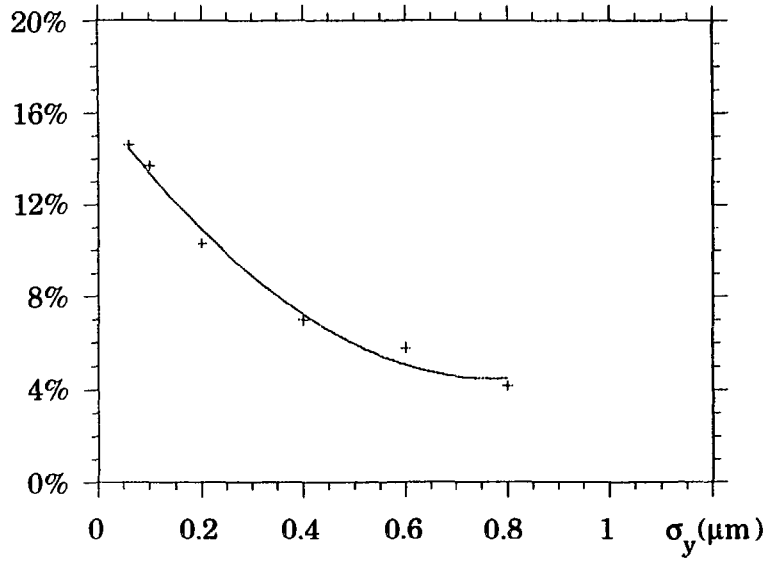

Figure 3 : The percentage of Ar^{2+} as function of the vertical beam size σ_y ($\sigma_x = 1\ \mu m$, $\sigma_z = 0.5$ mm and $N_e = 10^{10}$).

3. The space charge fields.

The space charge field of an electron bunch is attractive for positive ions. It constitutes a potential well in which the ions are trapped during the bunch passage.

At high energy the space charge field is mainly transverse due to the Lorentz contraction with respect to the rest system of the bunch. Its longitudinal variation follows the longitudinal distribution of the electrons, here assumed to be gaussian with a 0.5 mm r.m.s. value.

In the core of the bunch, the field increases proportionally to the distance from the beam axis in each tranverse direction. At long distance from the bunch the field decreases and follows a 1/r law. It also becomes independent of the beam tranverse dimensions.

The Figure 4a shows the variation of the vertical electric field with the distance along the vertical axis for different bunch aspect ratios. Similarly the Figure 4b shows the variation of the horizontal field along the horizontal axis.

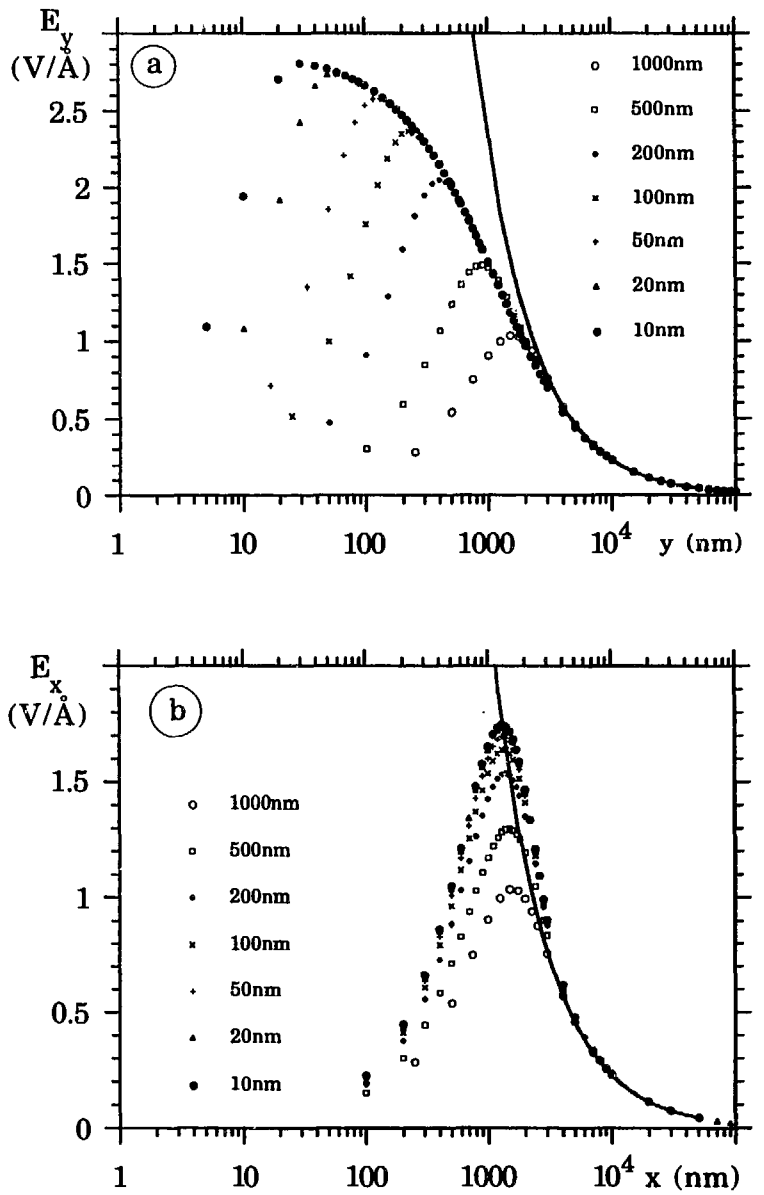

Figure 4 : Variation of the space charge electric field in the medium transverse plane of a gaussian bunch (σ_x = 1 μm, $N_e = 10^{10}$ and several σ_y indicated on the figure)
a) along the vertical axis (y),
b) along the horizontal axis (x).
The solid line shows the 1/r law of a line with the same charge density.

For a round electron bunch, with a gaussian distribution of r.m.s. value σ, the electric field E_r is radial and is given by :

$$eE_r = 2\, N_e r_e m_e c^2 \varphi(z)\, \frac{1 - e^{-\frac{r^2}{2\sigma^2}}}{r}$$

at a radial distance r and at a longitudinal position z in the electron bunch where the electron density is $\phi(z)$. N_e is the electron bunch population. The maximum field :

$$cE_{r\,max} = 2\, N_e r_e m_e c^2 \varphi(z)\, \frac{0.638}{\sqrt{2}\,\sigma}$$

is reached at a radial distance $r = 1.58\,\sigma$.

For a flat beam with an aspect ratio R, an analytic calculation shows (see Appendix III) that the horizontal field reaches its maximum on the x-axis at a distance x_m given by :

$$x_m \approx (1.307 + \frac{0.394}{R})\, \sigma_x$$

while the vertical field reaches its maximum on the y-axis at a distance y_m given by :

$$y_m \approx \sigma_y \left(\sqrt{2\, ln R} + \sqrt{\frac{\pi}{2}}\, \frac{1}{R} \right)$$

where R is the bunch aspect ratio. These expressions for x_m and y_m are still accurate to about 15 % for a round beam.

For the FFTB (10^{10} electrons per bunch and σ_x = 1 μm), the maximum electric field increases from 1 V/Å for a round beam to 1.7 V/Å on the horizontal axis and to 2.58 V/Å on the vertical axis for a flat beam with an aspect ratio of 20 (see Figure 5). Approximate expressions are given in Appendix III for these maximum fields. They saturate for very flat beams and reach a ratio $E_{x\,max}/E_{y\,max}$ of 0.610.

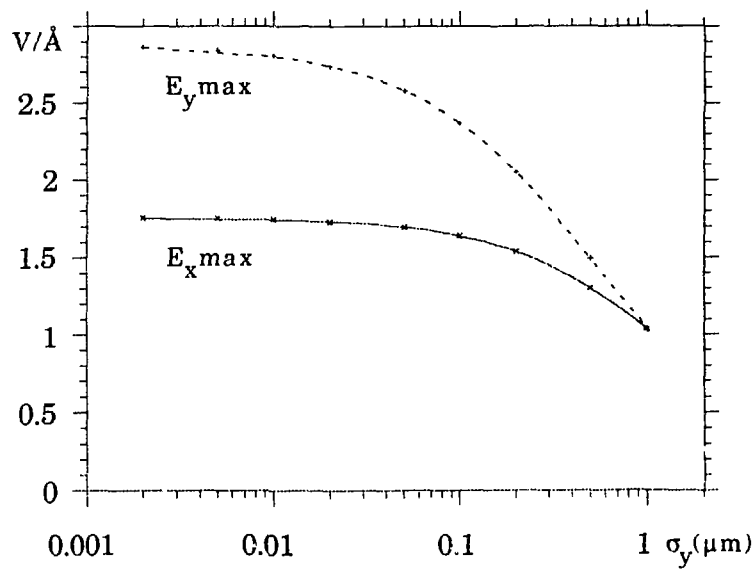

Figure 5 . The maximum electric field $E_{x\,max}$ along the horizontal axis and $E_{y\,max}$ along the vertical axis as function of the vertical beam dimension σ_y (σ_x = 1 μm, σ_z = 0.5 mm and $N_e = 10^{10}$).

It is worth noting that for very flat beams the vertical field on the vertical axis stays nearly constant from y_m to about $\sigma_x / 10$, but start to decrease above. This plateau only exists for aspect ratios larger than 25 (see Figure 4a).

The transverse magnetic field is proportional to the electric one : **B = E/c**. It gives a longitudinal kick proportional to the transverse velocity $v_\perp$ of an ion. It is shown in Appendix IV that the longitudinal tilt away from the transverse direction is :

$$\delta\alpha \approx \frac{v_\perp / c}{2\sqrt{1 - v_\perp^2 / c^2}}$$

As $v_\perp$ is of the order of 10^{-3}-10^{-4} of the light velocity for He and Ar ions, the longitudinal kick is a small effect.

On the opposite, the electrons, produced by ionization, are much more accelerated by the electric field, to velocities comparable with the light velocity. They are bent longitudinally in the backward direction by the magnetic force and they cannot reach the ion detectors.

It is also shown in the Appendix IV that there is a small longitudinal component of the electric field due to the beam divergence. It only gives a longitudinal tilt of the order of a few 10^{-4} rad.

4. Heavy Argon ions

Here, one considers a gas target of Argon atoms that have only a small displacement during the passage of an electron beam. For a qualitative discussion, one can only consider single ionization of Ar atoms into Ar^+, ignoring multiple ionization.

Once a Ar^+ ion has been created, it experiences the space charge field of the electron bunch. As stated in the Section 3 and the appendix IV, the longitudinal kick is negligible and one can only consider the transverse kick given by the transverse electric field.

One can also neglect the initial kinetic energy of the Ar^+ ion as it is a small fraction of the energy transfer in the ionization event, much smaller than the energy it will gain from the action of the electric field (of the order of one keV at least).

The kick given by the electric field depends on the transverse position of the ion and on the time of its creation (the ion will only experience the field of the electrons passing after). The final ion velocity has a wide spectrum ranging from zero (for ions created either on the beam axis or by the back of the electron bunch) to a maximum value. The latter corresponds to ions created by the head of the electron bunch at a position where the electric field is maximum.

Essentially, the maximum electric field and the maximum ion velocity increase when the electron density in the bunch increases, i.e. when the bunch dimensions decrease. The end point of the ion velocity spectrum is related to the bunch dimensions. The principle of the method is to determine this end point.

For a round beam the maximum ion velocity β_{max} (in units of light velocity) is obtained by integrating the maximum field over all the longitudinal bunch distribution :

$$\beta_{max} = 2\, N_e r_e m_e \frac{Z}{M} \frac{0.638}{\sqrt{2}\,\sigma}$$

for an ion of mass M and charge Z. With the FFTB parameters, $N_e = 10^{10}$ and $\sigma = 1$ μm and for Ar^+ ions, this formula gives $\beta_{max} = 3.5\ 10^{-4}$, corresponding to a 2.3 keV kinetic energy. It is proposed to obtain the ion velocities by measuring their time of flight (TOF) over the distance from the beam axis to the ion detector. The minimum time of flight is proportional to the transverse dimension σ and is numerically given by :

$$\tau_{min} \approx 0.1\ \mu sec/cm * \sigma(\mu m)$$

The simulated TOF spectrum (Figure 6) shows a sharp end point indicating that it could be easily determined if background is not too high.

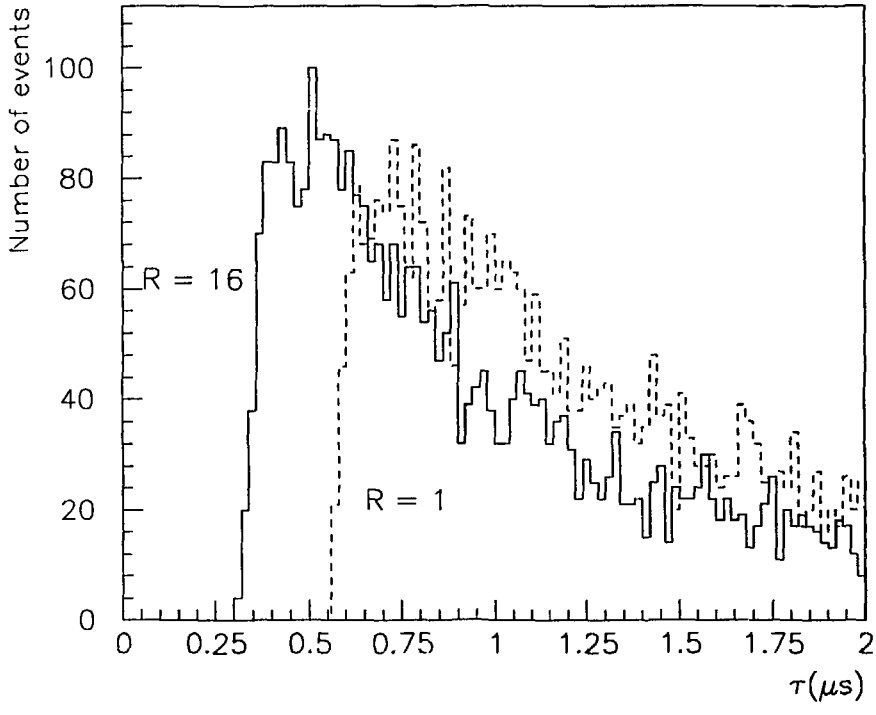

Figure 6 : The time of flight spectrum of 6000 Ar^+ ions for a 6 cm flight path and for two beam aspect ratios $R = \frac{\sigma_x}{\sigma_y}$ ($\sigma_x = 1$ μm, $\sigma_z = 0.5$ mm, $N_e = 10^{10}$).

The variation of the maximum ion velocity and of the minimum time of flight are shown on Figure 7 versus the beam dimensions, confirming the proportionality law.

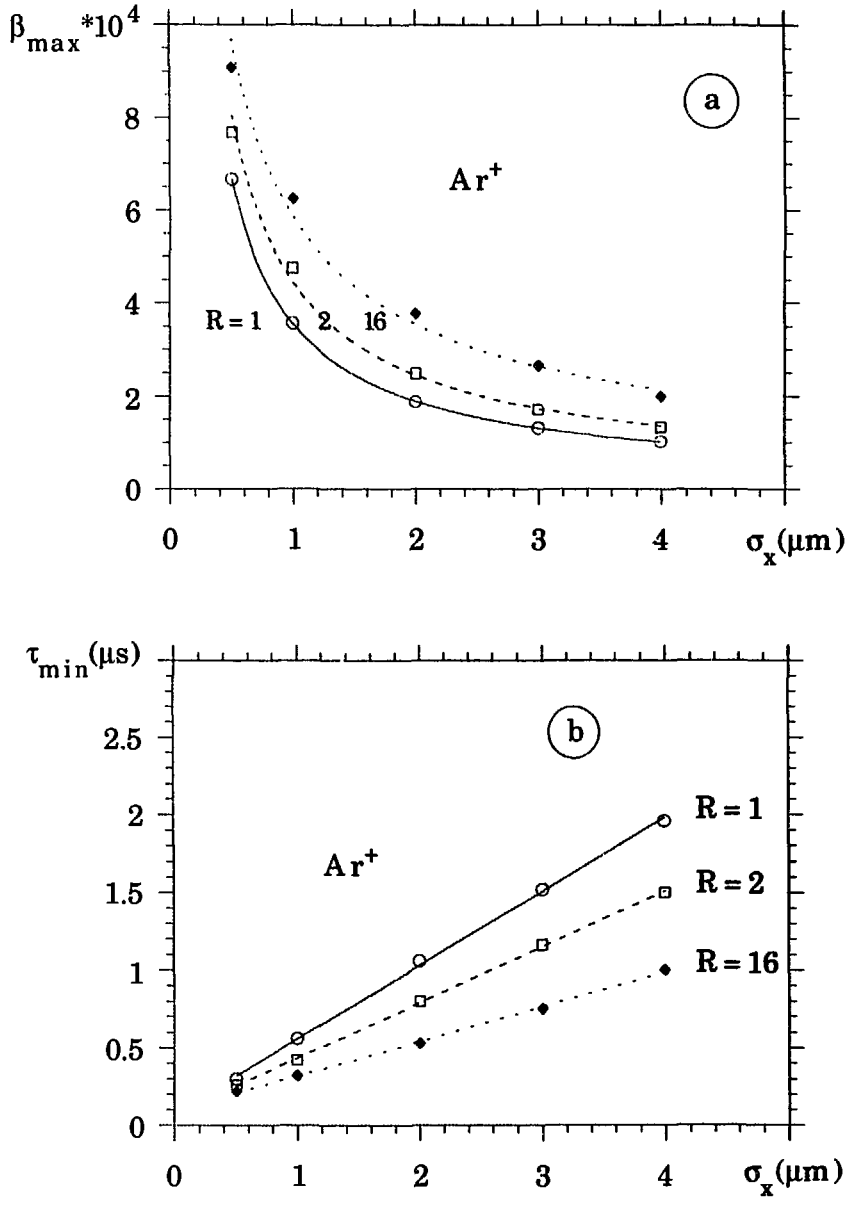

Figure 7 : Variation of : (a) the Ar^+ ion maximum velocity β_{max} in units of c,
(b) the minimum Ar^+ time of flight τ_{min} for a 6 cm flight path,
as function of the horizontal bunch dimension σ_X for different aspect ratios R.

Now, for a flat beam the maximum ion velocity also depends on the aspect ratio, but much less than on the horizontal dimension σ_x. The reason is the relatively smooth increase of the maximum field with the beam aspect ratio (see Figure 5). For instance, either a factor 16 increase of the aspect ratio or a factor 2 increase of σ_x gives approximately the same variation of the time of flight.

It is proposed to independently obtain the beam aspect ratio from the angular distribution of light ions (see Section 4). One can then correct the time of flight measurement to obtain the horizontal dimension.

The maximum velocity of Ar^{2+} ions is found to be just the double of the maximum velocity of Ar^{+} ions for a round beam. However, for a flat beam, the ratio of both maximum velocities is only about 1.6. Effectively, the ions have a displacement larger for Ar^{2+} than for Ar^{+} ions and due to the field gradient, the former experience a smaller field in average. Figure 8 shows the Ar^{+} ion displacement during the bunch passage. In average the displacement is much less than half an oscillation, confirming the initial assumption.

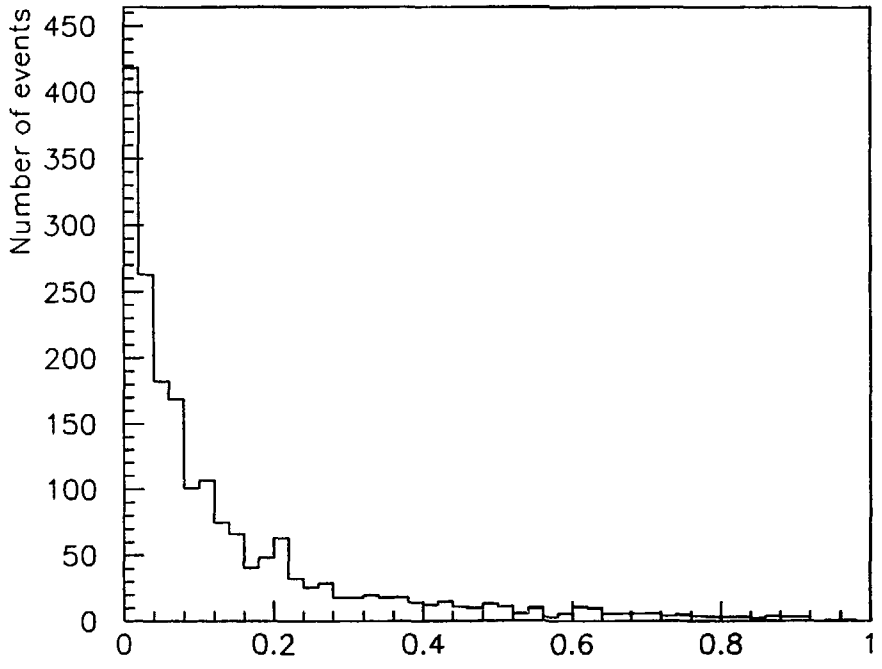

Figure 8 : Histogram of the Ar^{+} displacement in fraction of the initial ion distance to the beam axis. ($\sigma_x = 1\ \mu m$, $\sigma_y = 60$ nm, $\sigma_z = 0.5$ mm and $N_e \approx 10^{10}$).

To determine the end point of the Ar^{+} time of flight spectrum, one must discriminate the Ar^{2+} ions. It is proposed to give them a small longitudinal kick before detection (see Section 7). The produced displacement on the detector is proportional to their charge and inversely proportional to their energy. It is shown in Section 9 that a simultaneous measurement of the displacement and of the time of flight of each ion allows to achieve this discrimination.

This method can be used in the range of the FFTB dimensions, starting from the largest beam aspect ratio (about 16), up to a few–micron round beam. In particular a calibration, or at least a comparison, with a wire scanner would need to operate with round beams larger than one micron and less than 10^{10} electrons. The simulation shows that the front end of the Ar^+ time of flight spectrum is still sensitive to the beam radius, but the Ar^+ energy becomes very small (about 100 eV). It seems preferable to replace the Argon gas by a lighter gas as Helium. Figure 9 shows the variation of the He^+ minimum time of flight for such a beam of smaller electron density.

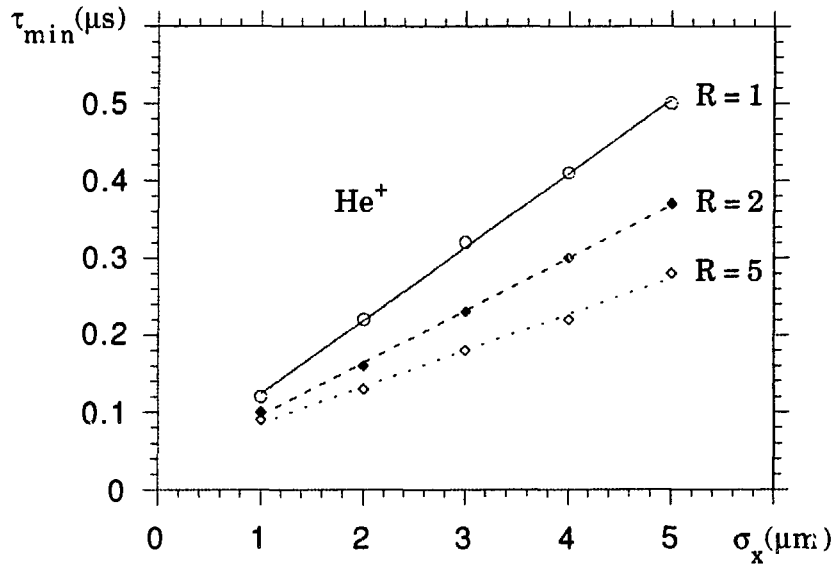

Figure 9 : The minimum time of flight of He^+ ions for different aspect ratios R and for $N_e = 5 \times 10^9$.

The angular distribution of the Ar^+ ions in the transverse plane (see Figure 11 b) shows a very weak dependence on the beam aspect ratio. For a flat beam, the maximum Ar^+ velocity shows only a slow variation with the direction of the emitted ion. As the electric field is larger in the vertical direction than in the horizontal one, vertically emitted ions have a larger flight path during the bunch passage. In particular ions created with a large impact parameter gain a vertical velocity comparable to the maximum horizontal velocity.

The time of flight has only a small variation with the longitudinal dimension of the bunch, as the kick received by the ion is proportional to the time integral of the field. The simulation indicates that the minimum time of flight increases by 12 % only when the length of a flat bunch (R=16) is doubled from 0.5 mm to 1 mm r.m.s..

A non-gaussian tail of the electron beam does not affect the minimum time of flight for a round beam as the maximum field is reached in the core of the beam (at 1.58 σ). The effect is still negligible for a flat beam and a tail having 7 % of the electrons between two and six standard deviations in x and y.

5. Light Helium ions

Here, one considers a gas target of Helium atoms that are ionized by the electron beam. The produced He^+, and in smaller quantity He^{2+}, ions are trapped and oscillate in the potential well of the bunch.

After passage of the electron bunch, they are emitted in the transverse plane with an angular distribution which is isotropic only in the case of a round beam. When the bunch is horizontally flat, the angular distribution becomes peaked in the horizontal transverse direction.

Using the simple model of a bunch with uniform density[4], the maximum ion velocity is proportional to the oscillation amplitude and to the square root of the focusing strength. The amplitude is the initial distance of the ion to the beam axis. In average the amplitude in one direction (horizontal or vertical) is proportional to the bunch dimension in that direction.

The horizontal and vertical amplitudes are in a ratio equal to the bunch aspect ratio $R = \sigma_x/\sigma_y$, while the corresponding focusing strengths are in the inverse ratio. Finally, the maximum horizontal and vertical ion velocities are in a ratio equal to $\sqrt{R}$, showing that the angular distribution of the detected ions should be peaked along the horizontal transverse direction for a flat beam.

Figure 10 shows the angular distribution of He^+ ions, folded in the angular interval $[-\pi/2, \pi/2]$, as given by the simulation code.

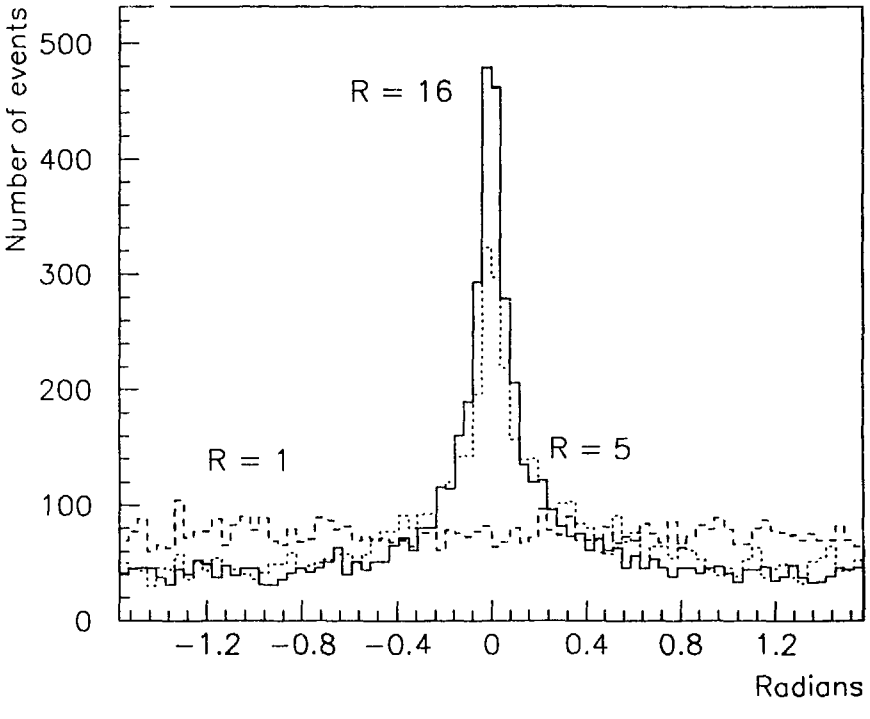

Figure 10 : The angular distribution of 6000 He^+ ions for three different beam aspect ratios R (the angle 0 corresponds to the horizontal direction)

(σ_x = 1 μm, σ_z = 0.5 mm and $N_e = 10^{10}$).

The angular anisotropy can be parametrized by the median $\theta_{1/2}$ that divides the [0, π/2] angular interval into two subintervals equally populated. The median $\theta_{1/2}$ is $\pi/4$ for a round beam and becomes smaller when the beam is horizontally flat.

Figure 11 shows the variation of the median $\theta_{1/2}$ with the bunch aspect ratio R for Helium and Argon ions. The sensitivity of the He^+ angular distribution to R does not depend very much on the ion velocity as indicated by varying the lower cut β_{min} applied on the velocity distribution. The sensitivity of Ar^+ is too small. The sensitivity of He^+ and Ar^{2+} are similar, but the latter has a poor statistics for small values of R.

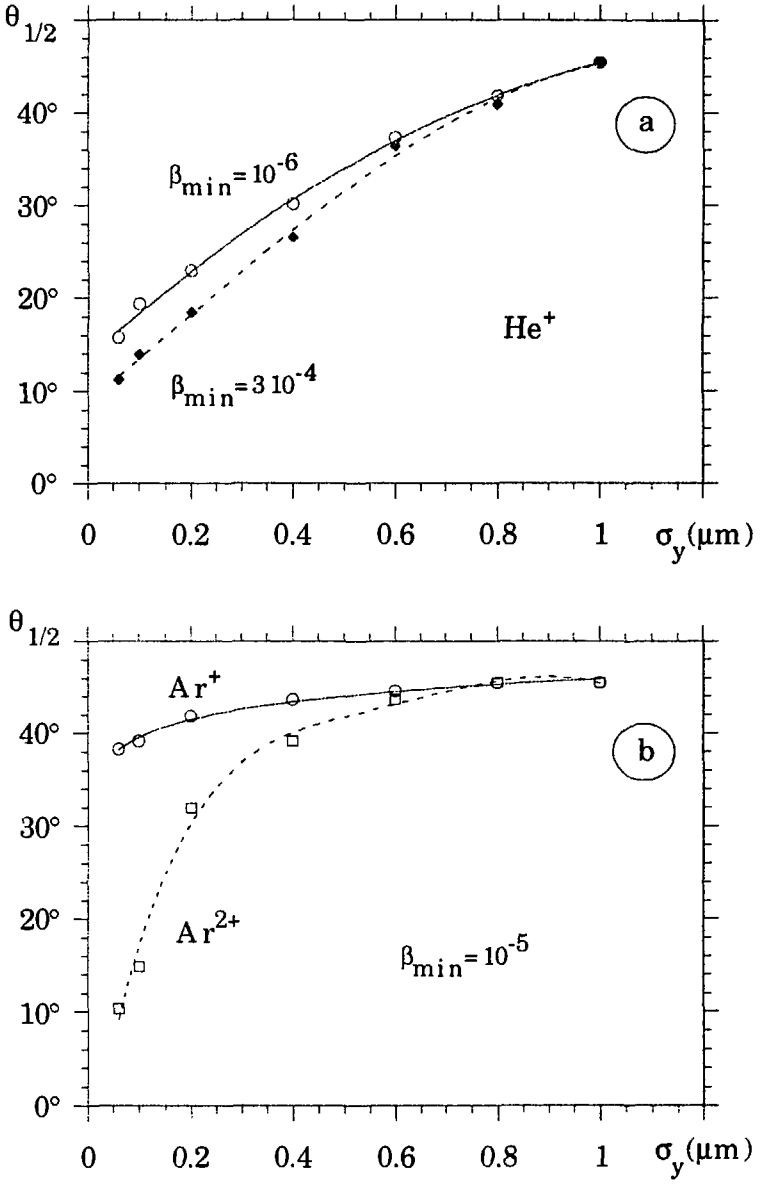

Figure 11 : The median $\theta_{1/2}$ versus the vertical beam size σ_y (a) for He^+ (b) for Ar^+ and Ar^{2+}
β_{min} is the smallest velocity of the selected ions (σ_x = 1 μm, σ_z = 0.5 mm, $N_e = 10^{10}$).

As the time of flight of Ar^+ ions (see Section 4), the angular distribution of He^+ has only a small dependence on the bunch length. The variation of $\theta_{1/2}$ is only a few percent when the bunch length is doubled.

6. The case of a positron beam.

When the FFTB is operated with positrons, instead of electrons, there is no difference in the primary ionization process. The first difference comes from the rate of ionization for Ar^+ ions. As ions are repelled from the bunch, the probability of successive ionizations is smaller, but only for flat beams (4.5 % less when R = 16).

For a round beam of one micron at least, there is no difference in time of flight of the ions. However, in case of a flat positron beam, vertically produced ions are repelled and pass through the region where the vertical field is maximum (above 2 σ_y). They gain larger velocities than in the case of a flat electron beam where they are attracted into the central region of lower field. The minimum time of flight τ_{min} is 20 % smaller for a R = 16 aspect ratio. The end point of the TOF spectrum (see Figure 12) is also sharper, making it even easier to determine than with electrons. The Figure 13 shows the variation of τ_{min} for a positron beam and Ar^+ ions.

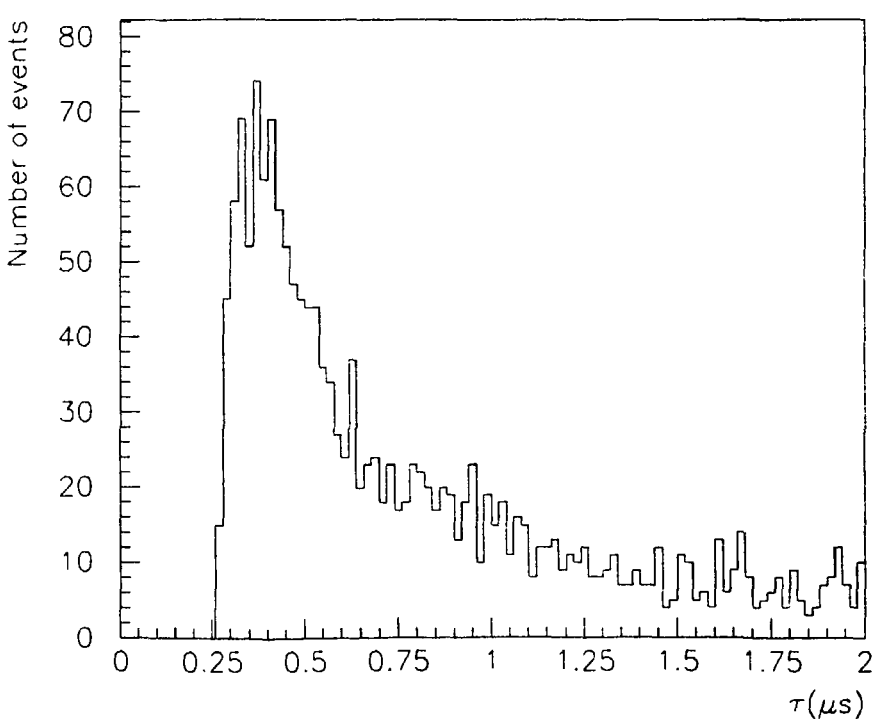

Figure 12 : Time of flight spectrum of 3000 Ar^+ ions for a 6 cm flight path (σ_x = 1 μm, σ_y = 60 nm, σ_z = 0.5 mm and of $N_e = 10^{10}$ positrons).

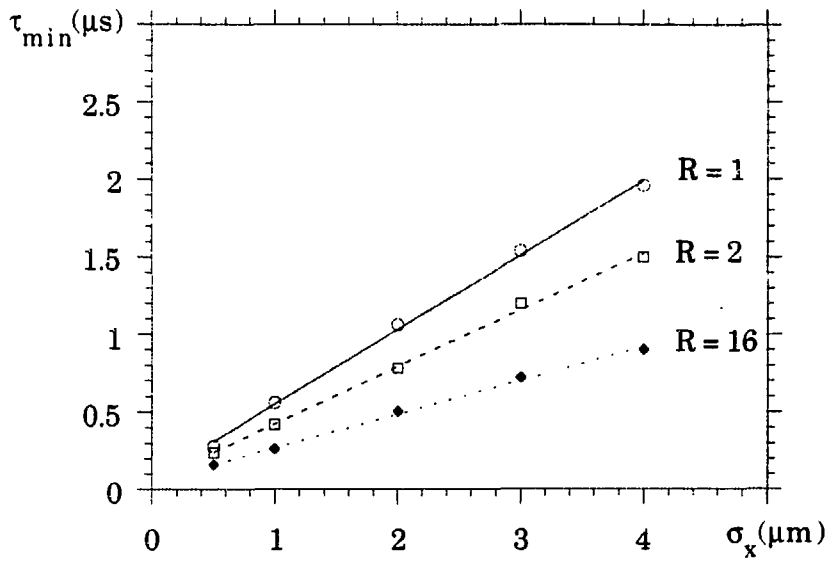

Figure 13 : Variation of the minimum Ar^+ time of flight τ_{min} for a 6 cm flight path, as function of the horizontal bunch dimension σ_x for different aspect ratios R.

Now, considering the angular distribution of Ar^+ and He^+ ions in the case of a positron beam, the larger vertical velocities reflects into a vertically peaked angular distribution. Unfortunately, this anisotropy is smaller than for electrons : Figure 14 shows the angular distribution of He^+ ions for an aspect ratio R = 16. The effect is three times smaller than with electrons.

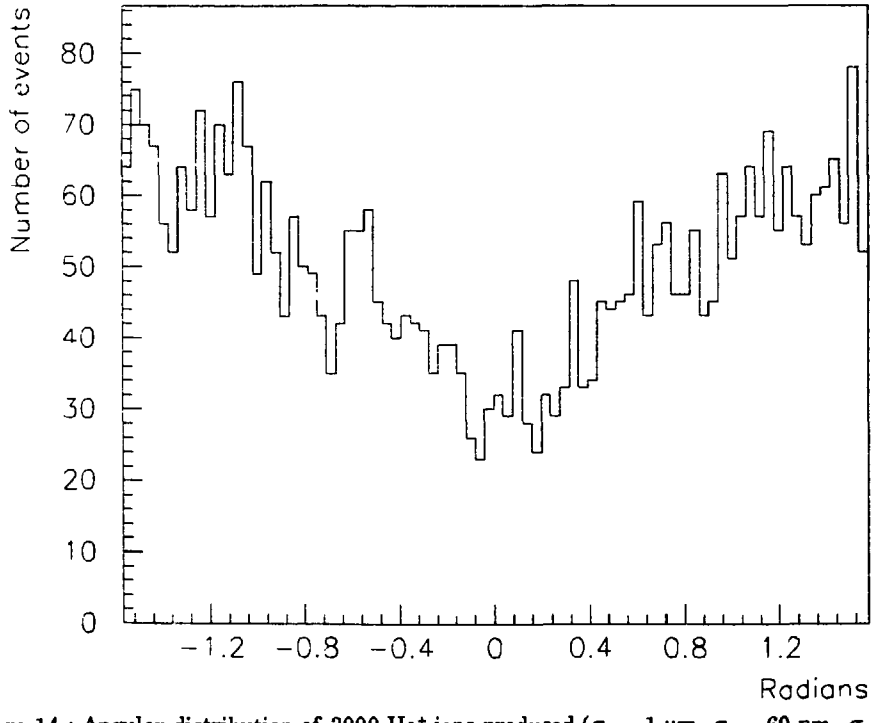

Figure 14 : Angular distribution of 3000 He^+ ions produced (σ_x = 1 μm, σ_y = 60 nm, σ_z = 0.5 mm and $N_e = 10^{10}$ positrons).

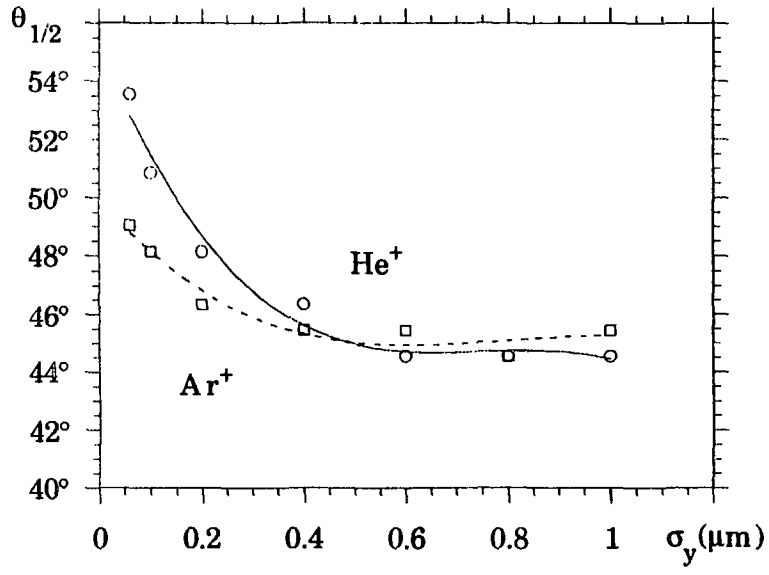

Figure 15 : The median $\theta_{1/2}$, parametrizing the angular distribution of He^+ and Ar^+ versus the vertical beam dimension σ_y ($\sigma_x = 1\,\mu m$, $\sigma_z = 0.5$ mm, $N_e = 10^{10}$ positrons).

Figure 15 shows the small variation of the angular distribution median $\theta_{1/2}$ with the vertical beam dimension.

In conclusion, for a positron beam, the proposed method to obtain the horizontal dimension by measuring the time of flight would work. But, the measurement of the angular distribution will not allow to obtain the aspect ratio R, apart for flat beams ($R \geq 5$). For nearly round beams, the bias on σ_x due to the uncertainty on R is about 30 % only.

7. The experimental set-up.

The proposed set-up of the Beam Size Monitor is made of a pulsed gas target and an array of ion detectors. Only the principle of the experimental set-up is given here.

7.1 The pulsed gas target.

Among several possibilities, the simplest device is a pulsed gas target contained in the beam pipe around the focus (see Figure 16).

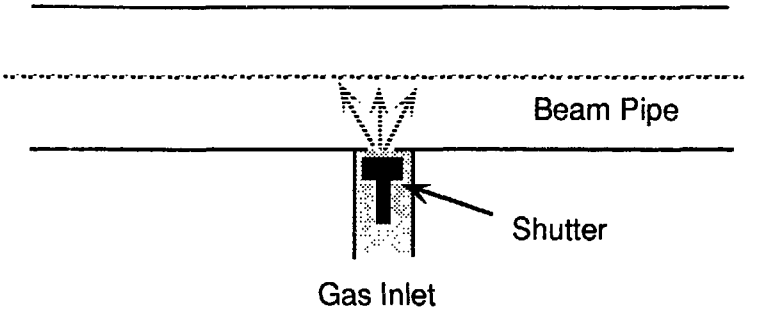

Figure 16 : Schematic view of the gas inlet and of the shutter to inject pulses of gas in the beam pipe at the focus.

A small hole (0.4 mm in diameter) in the wall of the pipe is closed by a shutter. A pulse of gas (about 100 μsec long) is injected just before the bunch passage by opening the shutter.

In a molecular regime, the structure of the gas jet is rapidly destroyed by reflections on the walls of the beam pipe (4 cm in diameter). One has more a gas target, filling the pipe section and extending a few centimeters longitudinally, than a gas jet.

A simulation, assuming diffusive reflection and negligible attachment on the walls, shows that the gas density at the focus is maximum 25 μsec after the shutter closing. It reaches 2.10^{12} Argon atoms per cm^3 for an inlet pressure of 2 Torr. The gas target extends longitudinally over 2.6 cm FWHM and over ± 4.5 cm total at that time.

A second hole allows to inject pulses of Helium. As the latter has a larger mean velocity, it diffuses through the hole faster than Argon. A larger gas density at the focus ($4*10^{12}$) can be reached with the same inlet pressure and hole cross-section. The maximum density is reached at the closing of the shutter and extends longitudinally over 3 cm FWHM and over ± 7 cm total .

The pulse of gas is pumped before the passage of the next bunch (100 msec after) through the beam pipe by two pumps (50 l/sec at 10^{-6}Torr) connected 30 cm upstream and downstream of the focus. The level of the residual pressure will be reached in a few milliseconds.

High gas purity is needed to avoid the adsorption of impurities on the pipe walls that would desorb later and would degrade the residual pressure in the pipe.

The most delicate part of the pulsed gas target is the shutter. On one hand, it must be fast (100-200 μsec opening). On the other hand, it must not transmit vibrations to the beam pipe.

7.2 The ion detector.

The ion detector consists of an array of eight pairs of microchannel plates (MCP) surrounding the beam focus at a distance of 6 cm (see Figure 17). Before reaching the MCP's the ions will pass through a narrow slit in a wolfram shielding 2 cm thick.

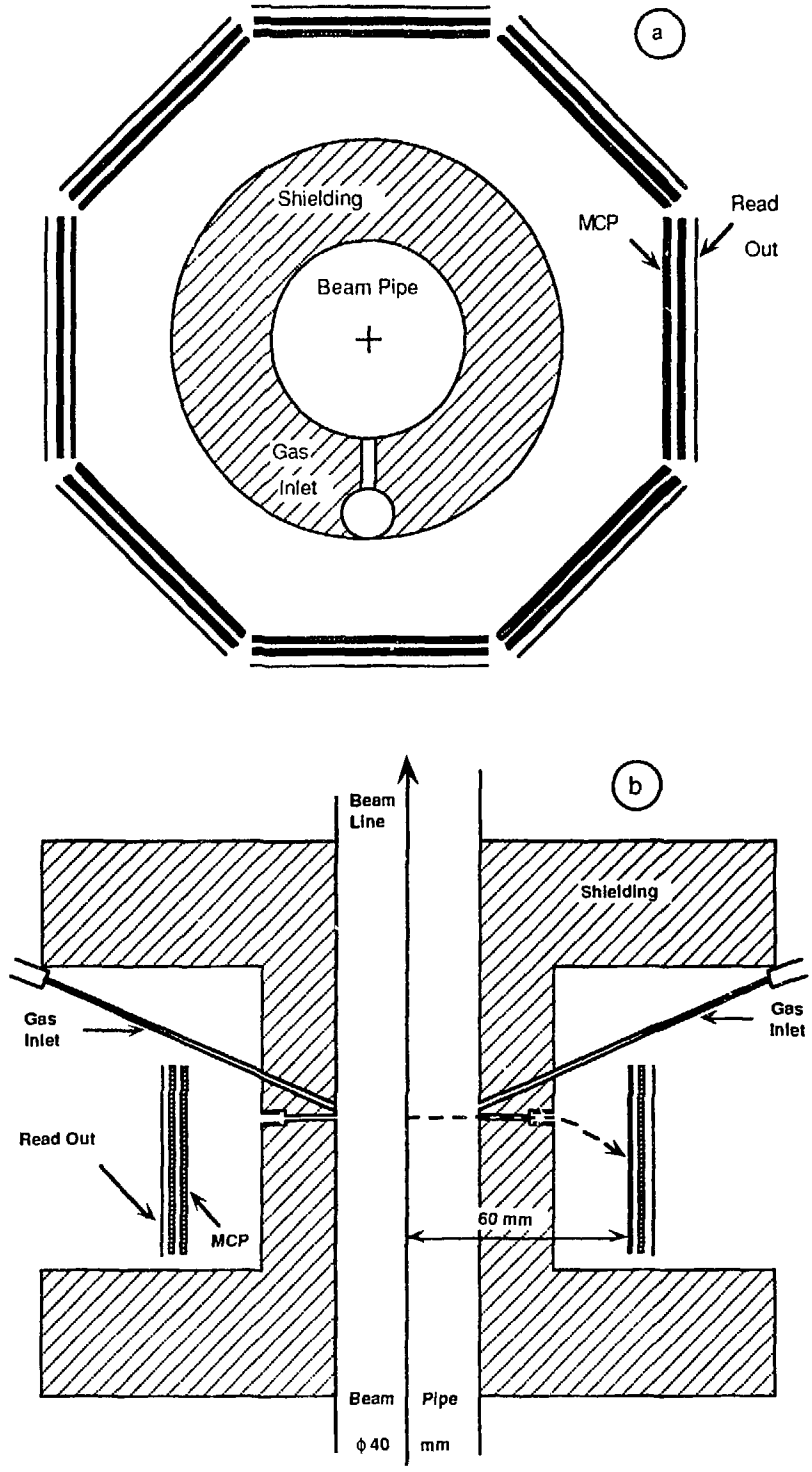

Figure 17 : Schematic view of the ion detector.
a) Transverse section at the FFTB focus.
b) Longitudinal section along the beam line.

The potential difference (≈ 2 kV) between the shielding and the front of the MCP's allows a final acceleration of the ions.

A small potential difference (≈ 100 V) across the slit in its second part gives a longitudinal kick to the Ar ions. The longitudinal displacement ζ of the ion impact on a MCP is proportional to its charge Z and inversely proportional to its kinetic energy. ζ is of the order of a few millimeters. The simultaneous measurement of ζ and of the time of flight for each ion allow to discriminate Ar ions of different charges (see Section 9).

The MCP's have a rectangular shape : 40x50x0.5 mm, with a hole diameter of 12 μm. The gain reaches about 3.10^3 at 1kV. A pair of MCP insures an overall gain of 10^7.

Each pair of MCP is read by nine parallel collectors (anode strips), as shown on Figure 18. The relatively large number of strips (72) is chosen to reduce the pile-up of signals, allowing fast measurements of the beam size. They give an angular resolution of 87 mrad. The number of strips will increased near the horizontal direction where the counting rate is peaked for flat beams and where one needs higher angular resolution.

To measure the longitudinal position of the ion impact, each anode strip is of a resistive type ($1k\Omega_{\square}$) allowing a charge division for this measurement. A 0.4 mm resolution is expected.

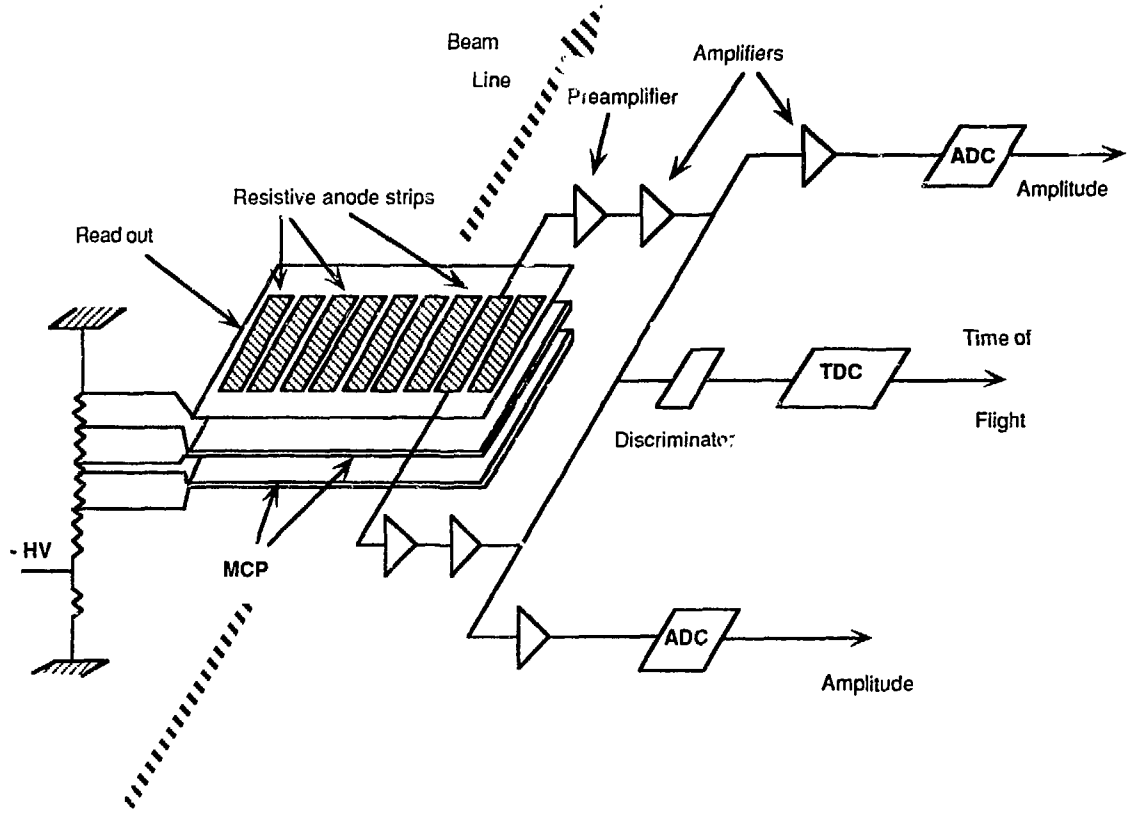

Figure 18 : Schematic view of a MCP pair with the anode strips and the associated electronics.

Signals collected on each side of the strips are amplified and analysed in time and amplitude by Time Digital Converters (TDC) and fast Amplitude Digital Converters (ADC) respectively. The comparison in amplitude of the two signals of one strip will determine the charge division between them and will give the longitudinal position ζ of the ion impact.

8. Backgrounds.

Three sources of background are considered here.

8.1 The fast elecromagnetic background.

Some fast particles, that are simultaneous with the beam passage, may hit the MCP's. These particles are mainly electrons of degraded energy, photons either from upstream showers or from scattered synchrotron radiation, and high-energy muons.

These particles will give signals in the MCP's that arrive much earlier than the signals of the ions. However, the restoring time of an hit channel of MCP is of the order of several milliseconds, due to its very high resistance. It cannot response to an ion arriving about one microsecond after. As the MCP's have a very long time constant, they cannot be blocked during the passage of the beam and of these fast background particles. To maintain a high efficiency of the MCP to detect the ions, the background level should be such that the occupancy of the channels would be at most a few percent.

It is very difficult to estimate what could be the background level. As experienced at SLC, it critically depends on the linac settings and on the beam transport in the FFTB line. One source of information is the background studies[10] of the microvertex detector of MARK II. There is about 0.1 hit per cm^2 and per burst. Half of the hits are believed to be charged particles of mostly about 0.5 GeV. The other half are thought to be photons, mostly from scattered synchrotron radiation.

Photons of synchrotron radiation will be absorbed in the shielding around the MCP's. It is expected that the shielding will also absorb a large part of the low-energy charged particles.

For instance, considering a flux of 0.05 charged particles per cm^2, assuming a 1/r decrease that gives a factor 1/2 for our MCP's and assuming an attenuation of 10 in the shielding, the flux on the MCP's is reduced to 0.0025 per cm^2 and per burst. Assuming again that 36 MCP channels will be fired per hit (6 strips per hit for the microvertex), with 4.4×10^5 channels per cm^2, the channel occupancy per pulse would be about 10^{-7} and would still be negligible if this background level is 4-5 orders of magnitude larger.

Moreover, the flux of 0.0025 per cm^2 and per burst will lead about 0.003 count per burst on each anode resistive strip. This rate would still be tolerable even if it would be ten times larger. In conclusion the electromagnetic background will be tolerable if its level is not much larger than in the Mark II experiment.

8.2 The slow neutron background.

The interaction of high-energy electrons in matter is the source of slow neutrons, of a few MeV energy with a long tail of higher-energy neutrons. In particular, the FFTB dump, 55 m downstream from the focus, will be an important source of slow neutrons[11]. High-energy electrons lost upstream in the FFTB line will be another source of slow neutrons.

By radiative capture, these neutrons produce γ-rays that may be detected by the MCP's, simulating ion hits.

The time of flight from the dump to the focus is two microseconds for 4 MeV neutrons and one microsecond for 16 MeV neutrons.

A shielding of the dump will likely be needed to reduce the neutron flux and their energy, in particular to measure beam dimensions of the order of two microns for a comparison with a wire scanner (see Figure 9).

8.3 The ions produced by synchrotron radiation in the gas target.

The gas target will also be ionized by the photons of synchrotron radiation emitted in the magnets of the FFTB line. Such ions produced in the region of high space charge field, i.e. close to the beam, will also be transversely kicked. As their space distribution is different from the distribution of the ions created by the electrons of the beam, their time of flight spectrum is also different. In particular, for a flat beam, in the vertical direction the field is maximum outside the core of the beam (above $2\sigma_y$). Ions produced there will gain maximum velocity and will populate the end point of the spectrum, but they cannot much bias its measurement.

The most important source of synchrotron photons, that are still close to the beam at the focus, is the last quadrupole QC1, 40 cm upstream. The last bending magnet BO3 gives a flux about ten times smaller.

For Argon an upper limit of their distance to the beam axis can be set to about 5 μm. Ions produced by photons passing at larger distance will receive a too small kick to populate the end point of the time of flight spectrum.

The photons passing at a distance lower than 5 μm are emitted in QC1 along an arc of the electron trajectory with a curvature $\alpha \approx 12.5$ μrad.

The number of such photons per electron is :

$$\frac{N_\gamma}{N_e} \approx \frac{\gamma}{100}\alpha = 1.25\ \%$$

These photons are emitted at the exit of QC1 by electrons that pass off axis. Considering that the electrons are at one standard deviation in average, the critical energy of the photon spectrum is about 40 keV.

The number of ions produced by the photons per atom is given by :

$$n_{ions} = \int \sigma_\gamma(u)\, n_\gamma(u)\, du$$

where $\sigma_\gamma(u)$ is the differential photo-ionization cross-section and $n_\gamma(u)$ is the spectral density of photons.

The photo-ionization cross-section is only significant in the lower part of the spectral density for a critical energy $u_c \approx 40$ keV. In that region the photo-ionization cross-section averaged on the spectrum is given by :

$$\langle\sigma\rangle = \frac{n_{ions}}{N_\gamma} = 1.34\, \frac{8}{15\sqrt{3}} \int \sigma_\gamma(\xi)\, \xi^{-2/3}\, d\xi$$

A numerical calculation, using experimental data, gives for Argon $\langle\sigma\rangle \approx 1$ Mb, that can be compared to the 2 Mb ionization cross-section σ_i by electrons.

Finally, for Argon the estimated signal/noise ratio ρ is :

$$\rho = \frac{N_\gamma}{N_e}\, \frac{\langle\sigma\rangle}{\sigma_i} \approx 0.6\%$$

For Helium the angular distribution will be measured for ions in a velocity interval larger, may be by a factor two. The upper limit of the distance can be set to 10 μm, instead of 5 μm. The number of photons per electron is doubled : 2.5 %.

Here again, it is found by numerical intregration that the photo-ionization cross-section averaged on the spectrum is nearly half the ionization cross-section by electrons, and the estimated signal/noise ratio ρ becomes 1.25 %.

9. Experimental resolution and operation.

The expected experimental resolution on the Ar^+ time of flight and on the charge separation has been studied with the simulation code. One has included finite gaussian errors on the measurements of the time of flight and of the longitudinal position of the ion impact on a MCP.

The accelerating voltage in front of the MCP's has been set to 1 kV and the field across the slit to 100 V/0.4 mm along a 1 cm path.

One has also added the effect of the finite length of the target seen by the ion detector. The beam dimension does not stay constant along this longitudinal length and has a waist at the FFTB focal point. With a 100 μm vertical β function, the vertical dimension is increased by a factor $\sqrt{2}$ for a ±100 μm longitudinal displacement. The finite length is fixed by tne width of the slit set to 0.4 mm.

Figure 19 shows the bidimensional plot of the two measured quantities : the time of flight τ and the longitudinal position ζ divided by τ^2. As ζ is proportional to the ion charge Z, but inversely proportional to the square of the velocity, ions of different charge should appear on different lines ζ/τ^2 = constant.

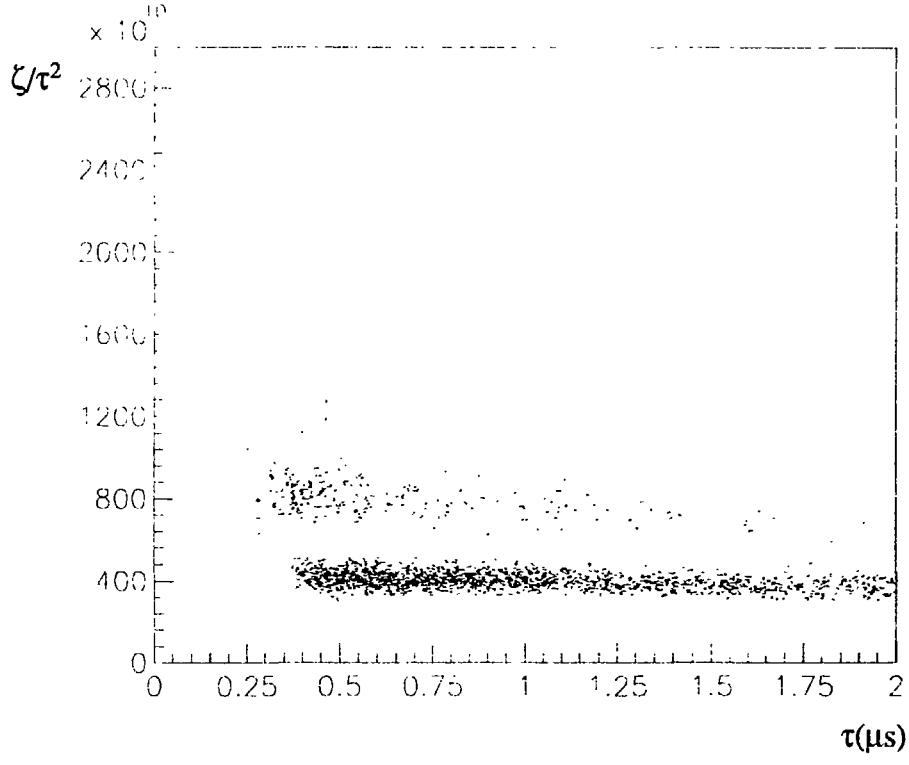

Figure 19 : Bidimensional plot of the measured quantities τ and ζ/τ^2 for Ar ions produced by an electron beam (σ_x = 1 μm, σ_y = 60 nm, σ_z = 0.5 mm and $N_e = 10^{10}$) with the experimental resolution given in the text.

With the assumed errors : 5 % r.m.s. on the time of flight and 0.5 mm r.m.s. on the longitudinal position, the different charges Ar^+, Ar^{2+} and Ar^{3+} are sufficiently separated (see figure 20).

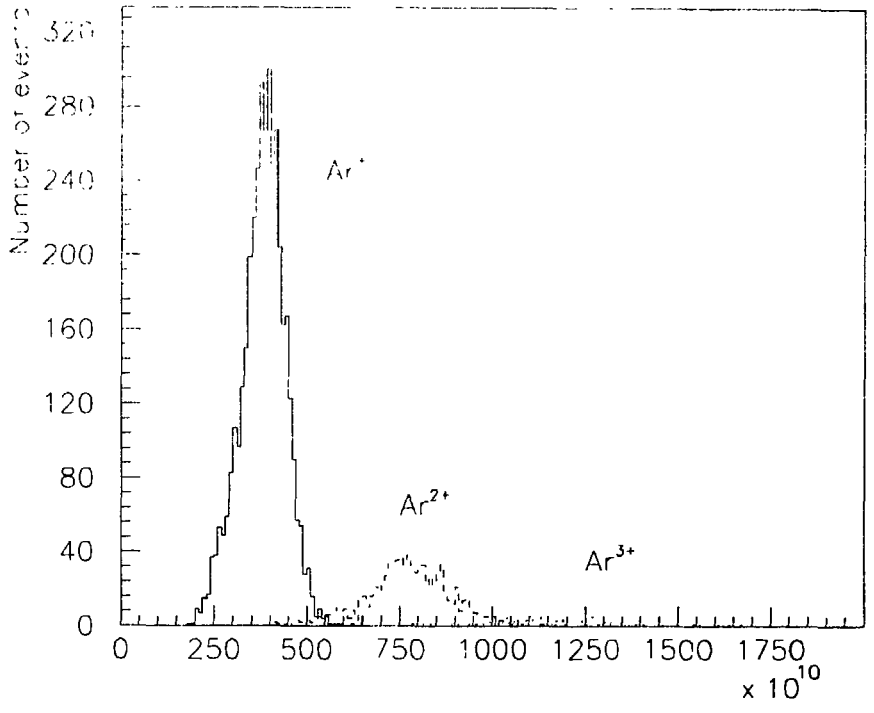

Figure 20 : The histogram of ζ/τ^2 for Ar ions, i.e. the projection of the bidimensional plot shown on the Figure 19.

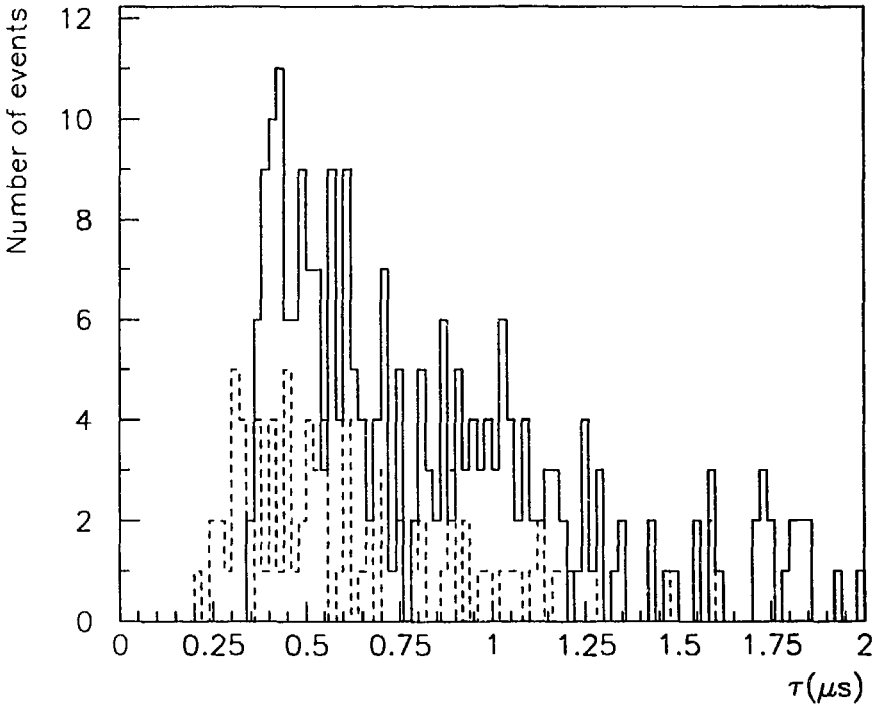

Figure 21 : The time of flight spectrum of 500 Ar^+ ions produced by an electron beam ($\sigma_x = 1\ \mu m$, $\sigma_y = 0.1\ \mu m$, $\sigma_z = 0.5$ mm and $N_e = 10^{10}$) with the experimental resolution given in the text.

——— Ar^+ ---- Ar^{2+}

The ion counting rate can be estimated from the gas target density and the ionization cross-section. For a gas density of 10^{12} atoms per cm^3 (i.e. a pressure P = 6.3 10^{-4} Torr) and a 2.0 Mb cross-section, 2000 Ar^+ ions are created per mm along the beam. Considering a ± 200 μm target length and a 20 % detection efficiency, about 150 ions would be detected by burst, enough to measure the beam radius with less than ten bursts.

Figure 21 shows the time of flight spectrum obtained with 500 ions.

The Helium ionization cross-section is about 7.5 times smaller than the Argon cross-section (see Table III). One would need to increase the gas density for a measurement in a few bursts. The production of He^{2+} is negligible (see Section 2) and there is no need to separate them.

Finally, the He^+ time of flight is much smaller than the Ar^+ one, as its mass is ten times smaller. The fastest He^+ will arrive 60 nsec after the bunch passage for a 6 cm flight path, and in the case of flat beam (R = 16).

The mode of operation could be first a few bursts with a pulse of Argon gas, followed by several bursts with pulses of Helium gas.

10. The case of a future e^+e^- linear collider with 200–250 GeV energy per beam.

One looks now at a possible extension of the above mentioned techniques to a future linear collider of 200 GeV to 250 GeV energy per beam such as the NLC (Next Linear Collider) proposed by SLAC[12].

Keeping a number of electrons $N_e = 10^{10}$ per bunch, the following beam dimensions to measure are chosen :

$$\sigma_x = 0.5\ \mu m \quad \sigma_y = 0.01\ \mu m \quad \sigma_z = 0.2\ mm$$

with a rather large aspect ratio R = 50 and again a gaussian distribution.

With these parameters the space charge electric field reaches values for which there will be tunnelling ionization of atoms. The velocity and angular distributions of the ions produced by this effect would have a poor representation of the initial bunch distribution. In order to get rid of this effect one foresees to only detect ions with a charge sufficiently high to be below the threshold of tunnelling ionization.

The tunnelling ionization is a stripping of atoms produced by a DC electric field[9]. Here, the stripping would be due to the space charge field of the electron bunch, that can be considered as DC at the scale of atomic frequencies. The atomic electrons can escape from the atoms through the potential barrier created by the external field.

The rate of the tunnel effect is given by [9]:

$$r = \frac{I}{\hbar}\sqrt{\frac{I}{\hbar\omega_t}}\; e^{-\frac{4}{3}\frac{I}{\hbar\omega_t}}$$

where the frequency ω_t, characteristic of the time of passage through the potential barrier, is taken as :

$$\omega_t = \frac{eE}{\sqrt{2mI}}$$

E and I being the electric field and ionization potential respectively.

The rate must be compared to the characteristic frequency associated with the atom crossing the bunch :

$$\nu = \frac{c}{\sqrt{2\pi}\,\sigma_z}$$

Due to the exponential behaviour, the threshold is rather sharp at r = ν, and may be considered in a first approximation as perfectly sharp.

In the case of FFTB the threshold is at E = 3.3 V/Å for Argon atoms (I = 15.76 eV) and at E = 6.3 V/Å for Helium atoms (I = 24.59 eV).

In the case of NLC, studied here, on the other hand, the maximum electric field is $E_y \simeq 13.7$ V/Å and would be the threshold of the tunnel effect for ions with a 40.8 eV ionization potential.

Then, to measure bunch dimensions, one can consider the following reactions produced as usual by resonant interaction of individual incident electrons :

(1)	Ar^{2+}	$\rightarrow Ar^{3+}$	I = 40.74 eV
(2)	Ne^{+}	$\rightarrow Ne^{2+}$	I = 40.96eV
(3)	He^{+}	$\rightarrow He^{2+}$	I = 54.42 eV

For reactions (1) and (2), by accident one sits just at the tunnel effect threshold which means that the bunch sizes given above are lower limits of the method. To reach smaller sizes, one has to use more ionized atoms, which makes the technique more involved. In the following, it is assumed that there is no contribution of the tunnel effect to the three reactions.

For instance, considering a gas target of Argon, one first notices that through tunnel effect, the neutral atoms are rapidly converted to Ar^{+} and Ar^{+} to Ar^{2+} in the region where the electric field is large. At maximum electric field, the production length of the Ar^{+} ion is 4×10^{-3} times the effective bunch length. For Ar^{2+} it is less than one hundreth of the effective bunch length and it can be considered that the bunch effectively crosses an Ar^{2+} target.

Then, Ar^{3+} ions are produced in the beam area, through the reaction (1) with a 0.56 Mb cross-section. However, an ionization saturation is reached in the case of the beam as explained in Section 2 and Appendix 1. It reduces the number of Ar^{3+} ions. For a slit of 0.4 mm width and a detection efficiency of 20 % (see Section 8) a rate of about 20 Ar^{3+} ions/burst is estimated.

One expects, and simulation confirms, about three vertical oscillations of the Ar^{3+} ions in the space charge field, leading to an angular distribution strongly peaked at the horizontal direction, even more peaked than the He^{+} angular distribution for the FFTB.

The beam size measurement relies on a good separation of Ar^{3+} from Ar^{4+}, and Ar^{2+} for the former. This involves certainly a greater sophistication of the proposed experimental set–up, such as an additional magnetic field to achieve a spatial separation of ions with different charges. That has not been studied yet.

In the case of a Neon gas target, Ne^{2+} ions are produced by reaction (2) with about the same cross-section as Ar ions by reaction (1). The situation is nearly the same for both reactions.

Finally in the case of an Helium gas target, the cross-section of reaction (3) is much smaller. However, there is no saturation of ionization and one can still expect about 10 ions per burst.

To conclude, the method proposed for the FFTB seems to be also possible for a 200-250 GeV per beam linear collider.

Appendix I

Simulation code for the generation and the motion of ions

The simulation code *"IONS"*, developped to study the principle of the beam size monitor, is divided into three parts : the first deals with the ion generation, the second one with the ion motion and the last one with the ion detector and its resolution.

i) Ion generation :

Ions are created at rest according to a space-time distribution (tranverse coordinates x and y, longitudinal coordinate z and time coordinate s = ct).

In the longitudinal direction z, the ions are uniformly created in a small interval around the focus point, corresponding to the effective length seen by the ion detector.

In the transverse plane, the space distribution can follow either a truncated gaussian law with r.m.s. values σ_x and σ_y or a uniform law inside a given ellipse. These r.m.s. values are corrected for the variation of the β-functions in the longitudinal interval.

To simulate the distribution of impact parameters each ion is transversely displaced by a random quantity b according to a $1/b$ law between given values b_{min} and b_{max}, apart in a fraction of the ions corresponding to Rutherford ionization events.

The time distribution also follows a truncated gaussian law. However, the created ions are only retained in proportion of the probability that the parent atoms have not been previously ionized. That probability w is calculated as function of the transverse position (x,y) and of the time $s = ct$ at which an ion is created.

$$w(x,y,s) = exp\left\{-\frac{\mu(x,y)}{2}\left(1 + \frac{Erf(s)}{Erf(s_{max})}\right)\right\}$$

where :

$$\mu(x,y) = \frac{\mu_0}{2\pi\, Ln\,\frac{b_{max}}{b_{min}}} \iint exp\left\{-\frac{(x + b\cos\theta)^2}{2\sigma_x^2} - \frac{(y + b\sin\theta)^2}{2\sigma_y^2}\right\}\frac{db\,d\theta}{b}$$

is the fraction of atoms that are ionized at the transverse position (x,y) for a gaussian distribution folded with the $1/b$ law of the impact parameters, and

$$\mu_0 = \frac{\sigma_i N_e}{2\pi\sigma_x\,\sigma_y}$$

is the fraction[5] of atoms that would be ionized by N_e electrons uniformly distributed in a transverse area $2\pi\,\sigma_x\sigma_y$.

The probability w of no previous ionization is small when μ_0 is large and ionization is saturated.

The gaussian law in transverse coordinates and in time are intended to simulate the electron distribution in the bunch. The truncation is usually set to three standard deviations or more.

Double-charge ions are generated in proportion of the cross-section for direct double ionization of an atom by a single interaction.

ii) Ion motion :

As the generation of ions is much faster than their tracking, it is convenient to have a higher statistics of generated ions than of the tracked ones. So, only a fraction of the generated ions is kept to simulate their motion in the space charge field of the electron bunch.

The transverse motion of the ion is calculated step by step with the Runge-Kutta integration method, using a routine "*FORCE*" that calculates the transverse components of the electric field. These components are expressed in terms of the complex error function as function of the transverse coordinates[13]. The longitudinal variation of the field is just the variation of the longitudinal electron density at the limit of very high energies.

At each step, the probability of the ion to be ionized again is calculated, by interpolation in a table prepared at the beginning[14]. That probability is proportional to $\mu(x,y)$, calculated with the corresponding ionization cross-section.

The tracking is stopped at the time corresponding to the truncation of the time distribution. Then the ion charge and its velocity components are stored.

According to Appendix IV, the small longitudinal tilt due to the magnetic force is just added at the end.

iii) Ion detection :

In order to optimize the detection of the ions and to study the performances of the proposed Beam Size Monitor, the motion of the ions to the MCP array and the experimental resolution are also simulated in the code. It allows to estimate the resolution on the end point of the time of flight spectrum and on the separation of the ions with different charges.

The time of flight to the MCP's is calculated taking into account the final acceleration required for maximum detection efficiency. A given gaussian error of measurement is added.

The longitudinal impact on the MCP's is calculated taking into account the longitudinal tilt given by a small electric field along the ion path in the slit, the initial longitudinal position z of the ion, and the small longitudinal kick given by the space charge magnetic force. A given gaussian error of measurement is also added.

Appendix II

Ionization cross-sections

II.1 Cross-section and impact parameter

Within Born approximation, the ionization of an atom by a relativistic electron results from the exchange of a virtual photon of energy ω and momentum $\boldsymbol{q}$. At ultrarelativistic energies, the exchanged photons become nearly real as their invariant momentum :

$$-q^2 = -\frac{\omega^2}{c^2} + q_{//}^2 + q_\perp^2 = \frac{-\omega^2}{\beta^2\gamma^2c^2} + q_\perp^2$$

is very small, in the same way as the transverse momentum $q_\perp$. The longitudinal momentum $q_{//}$ is :

$$q_{//} = \frac{\omega}{\beta c}$$

as obtained from the condition that the incident electron stays real (γ is the electron Lorentz factor and β is its velocity relative to the light velocity c).

Using the Weizsäcker-Williams approximation, the ionization cross-section is the product of the photoionization cross-section by the density of quasi-real photons accompanying the incident ultrarelativistic electron. This density is given by[15] :

$$\frac{d^2n}{d\omega\, dq_\perp^2} = \frac{\alpha}{\pi}\frac{1}{\omega}\frac{q_\perp^2}{\left(q_\perp^2 + \frac{\omega^2}{\beta^2\gamma^2c^2}\right)^2}$$

The photon density is maximum at $q_\perp = \frac{\omega}{\beta\gamma c}$ and $dn/dq_\perp$ scales like $\frac{1}{q_\perp}$ at large $q_\perp$.

The maximum of the photon density corresponds to the characteristic angle of photon emission $\theta \simeq \frac{1}{\gamma}$. The photon density vanishes along the longitudinal direction ($q_\perp = 0$), due to the transversality of real photons. Therefore the maximum roughly corresponds to a lower cut-off on momentum :

$$q_{\perp\, min}^{(0)} = \frac{\omega}{\beta\gamma c}$$

that vanishes at the limit of very high energies.

The differential ionization cross-section $d\sigma/d\omega$ is obtained after integration of the photon density over the transverse momentum $q_\perp$. Taking the maximum value of $q_\perp$ as the momentum of the ejected atomic electron considered as if it was free :

$$q_{\perp\, max} \approx \sqrt{2m\omega}$$

one obtains :

$$\frac{d\sigma}{d\omega} = \frac{\alpha}{\pi} \frac{\sigma_\gamma(\omega)}{\omega} Ln\left(\frac{2m_e c^2 \gamma^2}{\omega}\right)$$

where $\sigma_\gamma(\omega)$ is the photoionization cross-section.

This formula reproduces the well-known cross-section[6] of the resonant ionization at ultrarelativistic approximation. In particular it reproduces the relativistic and logarithmic rise with the electron energy, due to the decrease of the lower cut-off $q^{(0)}_{\perp min}$. It allows to calculate the ionization cross-section by electrons using experimental data on photoionization. It assumes no limitation on the coherence length of the exchanged photons, i.e. on their formation.

One must add the small contribution of the Rutherford scattering that involves a larger momentum transfer and that scales as $1/\omega^2$.

The relativistic rise of the resonant ionization cross-section is also interpreted as due to the distant collisions between the electron and the atoms. Effectively, the exchange of a transverse momentum $q_\perp$ corresponds to an impact parameter b roughly to $q_\perp$ related by the uncertainty relation :

$$b \cong \frac{\hbar}{q_\perp}$$

The lower cut-off $q^{(0)}_{\perp min}$ corresponds to a maximum impact parameter :

$$b_{max} \cong \beta\gamma \frac{\hbar c}{\omega}$$

that linearly increases with electron energy. At 50 GeV the maximum impact parameter is of the order of 1 mm (see Table I).

The upper cut-off $q_{\perp max}$ corresponds to a minimum impact parameter b_{min} of the order of the atomic radius as ω is of the order of the ionization potential ω_i.

Quantum calculation[16,17] shows that for impact parameters much larger than the minimum b_{min}, the spatial photon density $\frac{dn}{db}$ approximately varies as :

$$\frac{dn}{db} \approx \frac{b_{max}}{b} K_1^2\left(\frac{b}{b_{max}}\right)$$

where K_1 is the MacDonald function. For the FFTB the range of interest is of the order of the beam dimensions (0.1-1.0 μm). In this range the impact parameters b are such that $b_{min} << b << b_{max}$, and their distribution can be approximated by a $1/b$ law.

In the semi-classical picture, a finite time is needed for the exchanged photon to propagate from the incident electron to the atom. The photon must have been emitted by the electron at a time preceding its absorption by the atom[16]. This propagation time corresponds to a finite path of the electron (see Figure 22).

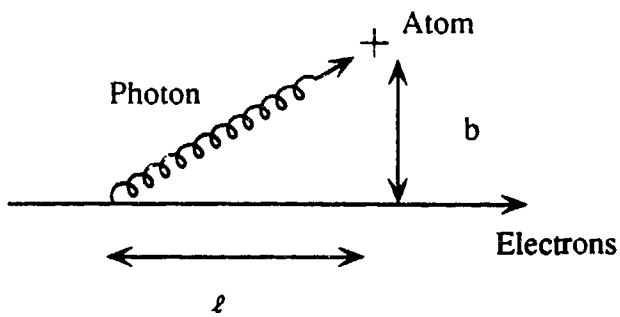

Figure 22 : Flight distance ℓ corresponding to the impact parameter b of an exchanged photon.

The order of magnitude of the flight distance for a real photon can be estimated as follows. In the rest system of the incident electron, the time of flight of a real photon over a distance b is :

$$\tau^* = \frac{b}{c}$$

In the laboratory system, this time is dilated by the Lorentz factor γ and the flight distance becomes :

$$l = \gamma c \tau^* = \gamma b$$

Along an infinitely long and linear electron trajectory, the maximum flight distance :

$$l_{max} \cong \gamma b_{max} = \beta \gamma^2 \frac{\hbar c}{\omega}$$

corresponds to the maximum impact parameter, as given by the density of equivalent photons in the radiation field. Therefore, l_{max} is also the coherence length of radiation in classical electromagnetism.

For maximum impact parameter values of about 1 mm (see Table I), the flight distance is of the order of 100 m at 50 GeV. However, this distance cannot be larger than the distance to the last bending of the electron trajectory, as the latter is usually much larger than the characteristic angle of radiation $\theta \approx 1/\gamma$. In the case of the FFTB line, the distance l^* to the last quadrupole is only about 40 cm, to which one adds a few centimeters to reach a point where the bending is larger than $1/\gamma$.

This maximum flight distance $l^* \approx 50$ cm will impose a lower maximum impact parameter $b^{(l)}_{max}$ and a higher minimum transverse momentum $q^{(l)}_{\perp min}$ than the values obtained above (see Table II). It will also reduce the ionization cross-section. In fact, the last bending and the interaction with the atoms of the target should be considered as a whole, and not separately, in a more correct treatment[8]. Moreover, the 50 cm path is in the vacuum of the beam pipe and there is no medium polarization (density effect) to consider.

In order to estimate this cut-off, the flight distance of the virtual photon must be evaluated by taking into account its small mass. In the laboratory system, the photon emission angle θ is :

$$\theta = \frac{q_\perp}{q_{//}} = \frac{q_\perp c}{\omega}$$

and the flight distance is given by :

$$l = \frac{b}{\theta} = \frac{\omega \hbar}{q_\perp^2 c}$$

using again $b \approx \hbar / q_\perp$.

The cut-off due to the finite length l^* is :

$$q^{(l)}_{\perp\, min} = \frac{1}{c}\sqrt{\frac{\omega \hbar c}{l^*}}$$

i.e. :

$$b^{(l)}_{max} = \sqrt{\frac{l^* \hbar c}{\omega}}$$

Correlatively, the differential cross-section of resonant ionization is reduced and given by :

$$\frac{d\sigma}{d\omega} = \frac{\alpha}{\pi} \frac{\sigma_\gamma(\omega)}{\omega} Ln\left\{\frac{2l^*}{\lambda\!\!\!^{-}_c}\right\}$$

where $\lambda\!\!\!^{-}_c$ is the Compton wavelength.

The cross-section does no more depend on energy, since the lower cut-off $q^{(0)}_{\perp min}$ is replaced by the energy-independent cut-off $q^{(l)}_{\perp min}$.

In conclusion, for FFTB and a dilute and thin gas target, the ionization process is dominated by distant electron-atom collisions. However, the flight distance of the exchanged photon is limited by the distance to the last quadrupole. Correspondingly, the maximum impact parameter is 60-70 μm only. It suppresses the relativistic rise of the cross-section and reduces it by 10-15 % in the case of FFTB.

It is worth noting that we have not considered the Stark effect produced by the space charge field of the beam. This effect may slightly increase the ionization cross-section.

II.2 Multiple ionization

Multi-charged ions can be produced for two reasons : either a single ionization event leads to a double-charge ion or successive single ionization events of the same atom lead to a multi-charged ion finally.

The former has a low probability, especially for Helium ($\sigma(He \rightarrow He^{2+}) \approx 445$ b). The latter is more important due to the high electron density in the bunch and the large ionization cross-section, especially for Argon.

With the same method as above, ionization cross-sections are related to the corresponding photoionization cross-sections by :

$$\sigma_{tot}(k \rightarrow k') = \frac{\alpha}{\pi} ln\left(\frac{2l^*}{\lambda\!\!\!^{-}_c}\right) \int_{\omega_k}^{\infty} \frac{\sigma_\gamma(k \rightarrow k')}{\omega} d\omega + \sigma_R$$

where :
* $\sigma_\gamma(k \rightarrow k')$ is the energy-dependent photoionization cross-section of a k-charged ion to a k'-charged ion ;
* ω_k is the threshold of photoionization of the k-charged ion ;
* σ_R is the Rutherford cross-section.

For production of multi-charged ions, it is enough to consider the following possibilities :

$He \rightarrow He^{2+}$ $\qquad$ $Ar \rightarrow Ar^{2+}$

$He^{+} \rightarrow He^{2+}$ $\qquad$ $Ar^{+} \rightarrow Ar^{2+}$

$Ar^{2+} \rightarrow Ar^{3+}$

In each case, one must calculate the sum rule : $\int_{\omega_k}^{\infty} \frac{\sigma_\gamma(\omega)}{\omega} d\omega$.

As He^{+} is an hydrogen-like ion, its photoionization cross-section is simply related to the cross-section of atomic hydrogen for which an exact calculation is availabie[18].

To our knowledge, there is no experimental data on photoionization cross-section of Ar^{+} and Ar^{2+} ions. We have used theoretical calculations[19] that only consider the photoionization of the outer 3p level. To get the total cross-section, we have assumed that photoionization of inner shells is not modified by the degree of ionization of the outer level. In addition, it is assumed that the Ar^{+} and Ar^{2+} ions are in their ground state before a new ionization, neglecting an excitation resulting from the preceding ionization. These assumptions limit the accuracy of the cross-section estimates.

Experimental data have been used for the case of the direct double photoionization of Helium[20] and Argon[21].

APPENDIX III

Calculation of the maximum electric field of a flat and Gaussian beam

The strength of the transverse electric field in a flat, gaussian and ultrarelativistic beam can be described by the Bassetti-Erskine formula[13]:

$$eE_x(x,y,z) = \frac{r_e mc^2 N_e}{\sigma_x \sigma_z} e^{-z^2/2\sigma_z^2} \, Im \;\; F(x,y)$$

$$eE_x(x,y,z) = \frac{r_e mc^2 N_e}{\sigma_x \sigma_z} e^{-z^2/2\sigma_z^2} \, Re \;\; F(x,y)$$

where

$$F(x,y) \simeq w\left(\frac{x+iy}{\sqrt{2}\sigma_x}\right) - e^{-(x^2/2\sigma_x^2 + y^2/2\sigma_y^2)} \, w\left(\frac{x/R + iRy}{\sqrt{2}\,\sigma_x}\right)$$

to an accuracy of the order of $1/R = \sigma_y/\sigma_x$. Here $w(z)$ is the complex error function.

The equations $\partial \, Im \, F(x,o) \,/\, \partial x = 0$ *and* $\partial \, Re \, F(o,y) \,/\, \partial y = 0$ give the locations x_m and y_m of the maximum fields E_{xm} along the horizontal x-axis and E_{ym} along the vertical y-axis respectively. These equations allow to express E_{xm} and E_{ym} as function of x_m and y_m respectively :

$$eE_{xm} = \frac{r_e mc^2 N_e}{\sigma_z} e^{-z^2/2\sigma_z^2} \sqrt{\frac{2}{\pi}} \frac{1}{x_m}\left[1 - \frac{1}{R} e^{-x_m^2/2\sigma_x^2}\right]$$

$$eE_{ym} = \frac{r_e mc^2 N_e}{\sigma_z} e^{-z^2/2\sigma_z^2} \sqrt{\frac{2}{\pi}} \frac{1}{y_m}\left[1 - \left(R + \frac{1}{R}\right) e^{-y_m^2/2\sigma_y^2}\right]$$

These expressions are valid to $\frac{1}{R}$ order. With this accuracy the locations x_m and y_m are given by :

$$\frac{x_m}{\sigma_x} = 1.307 + \frac{0.393}{R}$$

$$\frac{y_m}{\sigma_y} = \sqrt{2LnR} + \frac{1}{R}\sqrt{\frac{\pi}{2}}$$

Inserting these explicit expressions of x_m and y_m, one obtains :

$$eE_{xm} = \frac{r_e mc^2 N_e}{\sigma_x \sigma_z} e^{-z^2/2\sigma_i^2} \sqrt{\frac{2}{\pi}} \frac{1}{1.307}\left[1 - \frac{0.726}{R}\right]$$

$$eE_{ym} = \frac{r_e mc^2 N_e}{\sigma_x \sigma_z} e^{-z^2/2\sigma_i^2} \left\{1 - \frac{\sqrt{\pi}}{2R}\left[\sqrt{LnR} + \frac{1}{\sqrt{LnR}}\left(\frac{2}{\pi} + \frac{1}{2}\right)\right]\right\}$$

These maximum fields E_{xm} and E_{ym} are asymptotically independent of R, but the asymptotic values differ by a factor 0.610.

Appendix IV

The longitudinal motion

It is shown that the longitudinal kick P_z, given to a charged particle, is small compared to the transverse kick $P_\perp$.

Two effects contribute to the P_z value. The first results from the magnetic component of the field produced by the bunch in the laboratory frame. The second effect[22] arises from the angular divergence of the bunch.

i) The magnetic field effect :

If one neglects the beam divergence, the ratio of the longitudinal kick P_z to the transverse kick is approximatively given by :

$$\frac{P_z}{P_\perp} \cong \frac{v_\perp / c}{2\sqrt{1 - v_\perp^2 / c^2}}$$

where $v_\perp$ is the transverse velocity gained by the particle.

This general relation can be established by a study of the momentum transformation from the rest system of the bunch to the laboratory system. Let be δp_z^* and $\delta p_\perp$ the longitudinal and transverse momentum, transfered to the particle in the course of its motion, in the rest system. Its longitudinal momentum and its total energy are :

$$P_z^* = -\beta\gamma Mc + \delta p_z^*$$

$$E^* = \sqrt{M^2c^4 + (-\beta\gamma Mc + \delta p_z^*)^2 c^2 + \delta p_\perp^2 c^2}$$

where M is the mass of the particle, β is the electron bunch velocity in units of the light velocity c and γ is the related Lorentz factor.

In the laboratory system the transverse momentum is : $P_\perp = \delta p_\perp$. The longitudinal momentum is deduced using the Lorentz transformation law :

$$P_z = \gamma\left(P_z^* + \frac{\beta}{c} E^*\right)$$

To the second order in momentum transfer, one obtains :

$$P_z = \frac{1}{2}\frac{\delta p_\perp^2}{Mc} + \frac{\delta p_z^*}{\gamma}\left(1+\frac{1}{2}\frac{\delta p_z^*}{M\gamma c}\right)$$

In the transformation the contribution of the longitudinal transfer δp_z^* has been divided by γ and becomes much lower than the transverse one. The contribution of $\delta p_\perp$ is interpreted in the laboratory system as the action of the magnetic field, proportional to the transverse velocity. It is the main contribution that gives the expression given above.

The resulting expression is valid whatever the mass of the particle, for massive ions as well as for electrons.

ii) The beam divergence effect :

Assuming that the angular distribution of the electron trajectories is symmetric in x and y, the longitudinal component of the electron field is antisymmetric with respect to the transverse plane at the focus. The longitudinal component E_z vanishes in that plane and changes sign across it. However, the longitudinal momentum P_z given to an ion outside that plane by the finite E_z remains small in the case of FFTB.

For instance, using a Monte Carlo integration to evaluate the total electric field of a flat beam (σ_x = 1 μm, σ_y = 60 mm, β_x^* = 3 mm and β_y^* = 100 μm), and assuming that heavy ions are created with the same gaussian transverse distribution than the bunch and a longitudinal uniform distribution in the ± 0.2 mm interval, the dispersion of $\frac{P_z}{P_\perp}$ is only 0.4 mrad, with a vanishing average. With a larger transverse distribution of the ions, as expected from the finite impact parameters of ionization, the effect is still smaller (one obtains 0.1 mrad for a 1 μm transverse ion distribution in both directions x and y).

References

1) K. Brown et al. : "Proposal for Experimental Investigation of Final Focus Optical Systems for High-Energy e^+e^- Linear Colliders", May 25, 1989

2) J. Rees : SLAC-AP-24 (1984)

3) C. Prescott : SLAC internal memorandum, 1984 (unpublished)

4) J. Buon : Part. Accel. 31, 39 (1990), presented at the 14th Int. Conf. on High-Energy Accelerators, Tsukuba, 1989

5) P. Chen, D.L. Burke, M.D. Hildreth and R.D. Ruth : "A Plasma Beam Size Monitor", SLAC-AAS-41, 1988, presented at the International Workshop on the Next Generation of Linear Colliders, Stanford, 1988
P. Chen : SLAC-PUB-5186 (1990)

6) W.W. Allison & J.H. Cobb : Ann. Rev. Nucl. Part. Sci. 30 (1980) 253

7) F. Sauli : CERN 77-09 (1977)

8) X. Artru : private communication

9) L.V. Keldysh : Soviet Physics JETP, 20 (1965) 1307

10) R. Jacobsen et al. : SLAC-PUB-5205 (1990)
R. Jacobsen : private communication

11) D. Taylor : private communication

12) Proc. Int. Workshop on Next Generation of Linear Colliders, SLAC-REPORT 335 (December 1988)

13) B.W. Montague : CERN/ISR-GS/75-36
M. Basseti and G.A. Erskine : CERN/ISR-TH/80-06

14) P. Puzo : Rapport de stage (June 1990), in French.

15) V.B. Berestetskii, E.M. Lifshitz and P.L. Pitaevskii : "Quantum Electrodynamics", vol. 4 of Landau and Lifshitz Course of Theoretical Physics, Pergamon (1980) p.438

16) V.N. Baier, V.M. Katkov and V.M. Strakhovenko : Sov. J. Nucl.Phys. 36 (1982) 95

17) G.L. Kotkin, S.I. Polityko and V.G. Serbo : Sov. J. Nucl. Phys. 42 (1985) 440

18) J.A.R. Samson : Adv. At. Mol. Phys. 2 (1966) 237

19) M. Lamoureux, Thèse d'Etat, Orsay University (1979), in French
R.D. Chapman & R.J. Henry : The Astrophysical Journal 173 (1972) 243

20) J.M. Bizau : Thèse de 3ème Cycle, Paris VII University (1981), in french.

21) V. Schmidt et al. : Phys. Rev. A13 (1976) 1748

22) S. Kheifets, private communication

Acknowledgments :

We want to thank Pr. M. Davier, Director of LAL, for his continued encouragement. We are grateful to the FFTB international collaboration for his support. We are indebted to many people for fruitful discussions and we thank them all.